




Cite this: *J. Mater. Chem. A*, 2024, 12, 32981

# The impact of RGO and MWCNT/RGO on the microwave absorption of $\text{NiFe}_2\text{O}_4@ \text{Fe}_3\text{O}_4$ in the presence or absence of PANI

Farnaz Jamadi, Jamileh Seyed-Yazdi, \* Fatemeh Ebrahimi-Tazangi\* and Seyed Mohammad Hosseiny

This study investigates the impact of 1D (MWCNT) and 2D (RGO) carbonaceous structures on the microwave absorption performance of  $\text{NiFe}_2\text{O}_4@ \text{Fe}_3\text{O}_4$  nanocomposites decorated with/without PANI. These nanocomposites were fabricated using hydrothermal, coprecipitation, and *in situ* polymerization methods, resulting in various morphologies. The absorbers feature core@shell structures, 1D nanotubes, and 2D reduced graphene oxide layers, coated with polyaniline. These components contribute to quad-band absorption in the S, C, X, and Ku bands, with a maximum effective absorption bandwidth of 4.8 GHz for  $S_7$  at a matching thickness of only  $d = 1.6$  mm. The optimal reflection loss for  $S_5$  reaches  $\text{RL}_{\min}$  of  $-47.5$  dB at 4.6 GHz with a matching thickness of 4.6 mm, showing its best EAB of 4 GHz for  $d = 1.6$  mm. Additionally, CST simulation software demonstrates that the prepared materials effectively dissipate microwave energy in practical use. The impressive reflection loss and quad-band absorption are a result of the synergetic effects of various factors, such as core@shell structures, heterogeneous interfaces, multidimensional structures, and created defects. Analysis using the Smith chart confirmed the excellent impedance matching properties and strong electromagnetic wave attenuation of the conductive network of PANI/MWCNT/RGO, which collectively enhance the broadband absorption performance. The results of our study on MWCNT/graphene/polymer-based magneto-electric nanocomposite systems offer a promising foundation for the development of lightweight, high-performance microwave-absorbing materials with potential practical applications.

Received 14th June 2024

Accepted 15th July 2024

DOI: 10.1039/d4ta04128c

rsc.li/materials-a

## 1 Introduction

With the continuous and rapid advancement of electronic communication technology, popular intelligent electronic devices have brought convenience to people's lives, yet they also present a serious health risk due to the generation of electromagnetic (EM) pollution. In this era of telecommunications, many new electronic devices are being developed to address human needs, many of which operate at gigahertz frequencies. Various solutions have been proposed to mitigate concerns such as electromagnetic interference pollution, performance disruptions, and potential health hazards. One promising approach to addressing these issues involves utilizing absorbent materials, leading to significant research and development efforts in the realm of microwave-absorbing materials (MAMs).<sup>1–5</sup>

As a result, EM protective materials can incorporate magnetic substances like spinel ferrites ( $\text{MFe}_2\text{O}_4$ , where M represents elements such as Fe, Ni, Co, Cu, Zn, Mn, and Mg). Ferrites are

recognized for their chemical and thermal stability, as well as their adjustable absorption capabilities. These materials are renowned for their ferrimagnetic properties, which allow them to efficiently convert EM energy into thermal and various other forms of energy.<sup>6</sup> Nickel ferrite ( $\text{NiFe}_2\text{O}_4$ ) is distinguished by its exceptional properties, such as high resistivity, magnetic permeability, low coercivity, significant saturation magnetization, high anisotropy field, and corrosion resistance,<sup>7,8</sup> making it valuable for various applications like supercapacitors,<sup>9,10</sup> electrocatalysis,<sup>11</sup> and microwave absorption.<sup>12,13</sup> Its distinctive attributes also make it a suitable choice for use as soft magnetic materials in high-frequency applications.<sup>14,15</sup>

In various industries, magnetite ( $\text{Fe}_3\text{O}_4$ ) is commonly utilized as a magnetic loss microwave absorbent due to its high Curie temperature, strong spin polarization, affordability, and semi-metallic properties that make it suitable for microwave absorption applications. To enhance its dielectric loss capabilities,  $\text{Fe}_3\text{O}_4$  can be combined with conductive carbonaceous materials.<sup>16,17</sup>

Carbon-based materials such as graphene, graphene oxide (GO), reduced graphene oxide (RGO), and carbon nanotube (CNT) possess exceptional characteristics such as superior thermal conductivity, chemical stability, large specific surface

Department of Physics, Faculty of Science, Vali-e-Asr University of Rafsanjan, Rafsanjan, Iran. E-mail: j.seyedyazdi@gmail.com; fatemehebrahimi.edu2024@gmail.com

area, low density, thin profile, high conductivity, and inherent polarization.<sup>18,19</sup> High permittivity and electrical conductivities enable the formation of an interconnected network within nanocomposites, which enhances microwave absorption dissipation.<sup>20–23</sup>

Over the past few decades, significant research has focused on polymers, particularly conductive polymers like polyaniline (PANI), to develop composite materials with enhanced magnetic and dielectric attributes. PANI offers numerous advantages, such as excellent thermal, chemical, and environmental stability, high conductivity, lightweight nature, cost-effectiveness, and significant mechanical properties.<sup>24</sup> The high spin density of PANI<sup>25</sup> positions it as a promising candidate for combination with ferrites in MAMs. For example, Cai *et al.* synthesized an RGO/f-Fe<sub>3</sub>O<sub>4</sub>(1 : 10)@PANI composite that exhibited the best reflection loss of −46.49 dB at 9.93 GHz with a thickness of only 2.5 mm and a broadband of 4.25 GHz.<sup>17</sup>

Numerous studies have explored the properties of ferrites and carbon-based materials. For example, Ebrahimi-Tazangi *et al.* synthesized α-Fe<sub>2</sub>O<sub>3</sub>@CoFe<sub>2</sub>O<sub>4</sub>/GO nanocomposites *via* the hydrothermal method, decorating the GO surface with two ratios (3 : 1) and (5 : 1) to GO. Their (5 : 1) sample exhibited the highest reflection loss of −81.24 dB at 11.98 GHz, with a thickness of 1.4 mm and a broadband of 3.78 GHz.<sup>26</sup> Moreover, Zhang *et al.* combined carbon nanofibers with cobalt ferrite, leading to outstanding microwave absorption properties. The composite demonstrated a maximum reflection loss of −137 dB at 11.3 GHz with a thickness of 2.6 mm.<sup>27</sup> Additionally, Ma *et al.* hydrothermally synthesized spherical RGO/ZnFe<sub>2</sub>O<sub>4</sub>/Ni nanohybrids and achieved an optimal reflection loss of −22.57 dB at 4.2 GHz with a thickness of 2.5 mm and a broadband of 6.6 GHz.<sup>28</sup> Li *et al.* achieved a notable reflection loss of −76.5 dB at 7.9 GHz for MnFe<sub>2</sub>O<sub>4</sub>/RGO/Diatomite, with an effective bandwidth of 3.6 GHz, using a 2.5 mm thickness.<sup>29</sup> Previous research suggests that utilizing nanostructures with heterogeneous multi-layers can enhance absorption performance. Therefore, in this study, various multi-component MAMs comprising NiFe<sub>2</sub>O<sub>4</sub>/Fe<sub>3</sub>O<sub>4</sub>/PANI, NiFe<sub>2</sub>O<sub>4</sub>/Fe<sub>3</sub>O<sub>4</sub>/PANI/MWCNT, NiFe<sub>2</sub>O<sub>4</sub>/Fe<sub>3</sub>O<sub>4</sub>/PANI/RGO, NiFe<sub>2</sub>O<sub>4</sub>/Fe<sub>3</sub>O<sub>4</sub>/RGO/MWCNT, and NiFe<sub>2</sub>O<sub>4</sub>/Fe<sub>3</sub>O<sub>4</sub>/PANI/RGO/MWCNT were synthesized through different methods. The structural, morphological, magnetic, and microwave absorption properties of these nanocomposites were thoroughly investigated.

## 2 Experimental

### 2.1 Materials

Ni(NO<sub>3</sub>)<sub>2</sub>·6H<sub>2</sub>O, Fe(NO<sub>3</sub>)<sub>2</sub>·9H<sub>2</sub>O, NH<sub>4</sub>·OH, FeCl<sub>2</sub>·4H<sub>2</sub>O (purity: 99.99%), FeCl<sub>3</sub>·6H<sub>2</sub>O (purity: 98%), PANI, RGO, multi-walled carbon nanotubes (MWCNT), ammonia, hydrochloric acid (HCl), ethanol (ET) (99.9%), (NH<sub>4</sub>)<sub>2</sub>·S<sub>2</sub>O<sub>8</sub> (ammonium persulfate), were obtained from Merck (Germany).

### 2.2 Synthesis of NiFe<sub>2</sub>O<sub>4</sub> (S<sub>1</sub>)

NiFe<sub>2</sub>O<sub>4</sub> was synthesized using the hydrothermal method. Initially, 50 mmol of Fe (NO<sub>3</sub>)<sub>2</sub>·9H<sub>2</sub>O and 25 mmol of Ni

(NO<sub>3</sub>)<sub>2</sub>·6H<sub>2</sub>O were dissolved in 76 mL of deionized (DI) water and stirred separately for 20 minutes. Subsequently, ammonia solution was dropwise added to the mixture while stirring for 1 hour to adjust the pH of the precursor solution to 11. After ultrasonication of the mixed solution for 1 hour, it was transferred into a 250 mL Teflon-lined stainless steel autoclave and sealed. The autoclave was then heated to 180 °C and maintained at this temperature for 24 hours for the hydrothermal reaction. After the reaction, the autoclave was allowed to cool to room temperature. The resulting product was washed five times with ethanol and DI water to achieve a neutral pH of 7. Finally, the sample was separated using a magnet and dried at 40 °C for 6 hours.

### 2.3 Synthesis of NiFe<sub>2</sub>O<sub>4</sub>/Fe<sub>3</sub>O<sub>4</sub> (S<sub>2</sub>)

NiFe<sub>2</sub>O<sub>4</sub>/Fe<sub>3</sub>O<sub>4</sub> was prepared using the co-precipitation method. Initially, 0.75 g of NiFe<sub>2</sub>O<sub>4</sub> was dissolved in 100 mL DI water, stirred for 30 minutes, and subjected to ultrasonication for 40 minutes. Subsequently, the solution was placed in an oil bath at 75 °C, and 2.6 g of FeCl<sub>3</sub>·6H<sub>2</sub>O and 1.6 g of FeCl<sub>2</sub>·4H<sub>2</sub>O were added. The mixture was stirred for 30 minutes under a nitrogen atmosphere. Following this, 15 mL of ammonia was added dropwise to the solution under the same conditions, and the solution was heated and stirred for an additional two hours. Finally, the resulting product (S<sub>2</sub>) was collected using a magnet, washed with ethanol and DI water until reaching a neutral pH of 7, and then dried.

### 2.4 Synthesis of NiFe<sub>2</sub>O<sub>4</sub>/Fe<sub>3</sub>O<sub>4</sub>/PANI (S<sub>3</sub>)

Initially, 1.4 g of NiFe<sub>2</sub>O<sub>4</sub>/Fe<sub>3</sub>O<sub>4</sub> was dissolved in 100 mL of DI water and sonicated for 35 minutes. A solution was prepared by adding 0.33 mL of HCl to 100 mL of DI water. Following this, the HCl solution was combined with the solution containing NiFe<sub>2</sub>O<sub>4</sub>/Fe<sub>3</sub>O<sub>4</sub>, and 0.7 g of aniline was added dropwise. The mixture was dispersed using ultrasonication for 60 minutes and subsequently placed in an ice bath at 0–5 °C with continuous stirring for an additional 60 minutes. Finally, 0.7 g of ammonium persulfate dissolved in 60 mL of water was added to the mixture, and the resulting mixture was stirred for 7 hours at 0–5 °C. After collection using a magnet, washing with DI water and ethanol, the product was dried.

### 2.5 Synthesis of NiFe<sub>2</sub>O<sub>4</sub>/Fe<sub>3</sub>O<sub>4</sub>/PANI/RGO (S<sub>4</sub>)

The initial step involved dissolving 0.3 g of NiFe<sub>2</sub>O<sub>4</sub>/Fe<sub>3</sub>O<sub>4</sub>/PANI in 100 mL of deionized (DI) water and dispersing it using ultrasonication. Subsequently, 0.1 g of RGO was dissolved in a mixture of 100 mL of DI water and ethanol. The first solution and the RGO solution were then combined and stirred for 24 hours. The synthesis of NiFe<sub>2</sub>O<sub>4</sub>/Fe<sub>3</sub>O<sub>4</sub>/PANI/MWCNT (S<sub>5</sub>) was carried out using the same procedure.

### 2.6 Synthesis of NiFe<sub>2</sub>O<sub>4</sub>/Fe<sub>3</sub>O<sub>4</sub>/RGO/MWCNT (S<sub>6</sub>)

0.3 g of NiFe<sub>2</sub>O<sub>4</sub>/Fe<sub>3</sub>O<sub>4</sub> was dissolved in 100 mL of DI water. Subsequently, 0.05 g of RGO and 0.05 g of MWCNT were dissolved in a mixture of 25 mL of DI water and 75 mL of ethanol,

and the solution was dispersed using probe sonication for 30 minutes. Finally, the two solutions were combined and stirred for 24 hours using a magnetic stirrer.

### 2.7 Synthesis of $\text{NiFe}_2\text{O}_4/\text{Fe}_3\text{O}_4/\text{PANI}/\text{RGO}/\text{MWCNT}$ ( $\text{S}_7$ )

0.3 g of  $\text{NiFe}_2\text{O}_4/\text{Fe}_3\text{O}_4/\text{PANI}$  was dissolved in 100 mL DI water. Subsequently, 0.05 g of RGO and 0.05 g of MWCNT, previously dissolved in a mixture of DI water and ethanol and dispersed, were combined. The resulting materials were then stirred for 24 hours using a magnetic stirrer and subsequently dried.

The prepared samples, namely  $\text{NiFe}_2\text{O}_4$ ,  $\text{NiFe}_2\text{O}_4/\text{Fe}_3\text{O}_4$ ,  $\text{NiFe}_2\text{O}_4/\text{Fe}_3\text{O}_4/\text{PANI}$ ,  $\text{NiFe}_2\text{O}_4/\text{Fe}_3\text{O}_4/\text{PANI}/\text{RGO}$ ,  $\text{NiFe}_2\text{O}_4/\text{Fe}_3\text{O}_4/\text{PANI}/\text{MWCNT}$ ,  $\text{NiFe}_2\text{O}_4/\text{Fe}_3\text{O}_4/\text{RGO}/\text{MWCNT}$ , and  $\text{NiFe}_2\text{O}_4/\text{Fe}_3\text{O}_4/\text{PANI}/\text{RGO}/\text{MWCNT}$ , are designated as  $\text{S}_1$ ,  $\text{S}_2$ ,  $\text{S}_3$ ,  $\text{S}_4$ ,  $\text{S}_5$ ,  $\text{S}_6$ , and  $\text{S}_7$ , respectively. The steps involved in the preparation of the nanocomposite samples are illustrated in Fig. 1.

## 3 Results and discussion

X-ray diffraction (XRD) analysis was conducted to determine the phases present in the prepared samples. Fig. 2 displays the XRD patterns of samples  $\text{S}_1$ ,  $\text{S}_2$ ,  $\text{S}_3$ ,  $\text{S}_4$ ,  $\text{S}_5$ ,  $\text{S}_6$ , and  $\text{S}_7$ . In the XRD spectrum of  $\text{NiFe}_2\text{O}_4$ , peaks at  $2\theta = 30.3^\circ$ ,  $35.7^\circ$ ,  $43.4^\circ$ ,  $53.8^\circ$ ,  $57.4^\circ$ , and  $63^\circ$  are respectively indexed to the (220), (311), (400), (422), (511), and (440) crystal planes, indicating the cubic spinel structure of  $\text{NiFe}_2\text{O}_4$ .<sup>15</sup> The sharpness of the XRD peaks suggests well-crystallized nanoparticles. Additionally, Bragg peaks at  $2\theta = 18.4^\circ$ ,  $30.2^\circ$ ,  $35.5^\circ$ ,  $43.2^\circ$ ,  $53.7^\circ$ ,  $57.2^\circ$ ,  $62.4^\circ$ , and  $74.3^\circ$

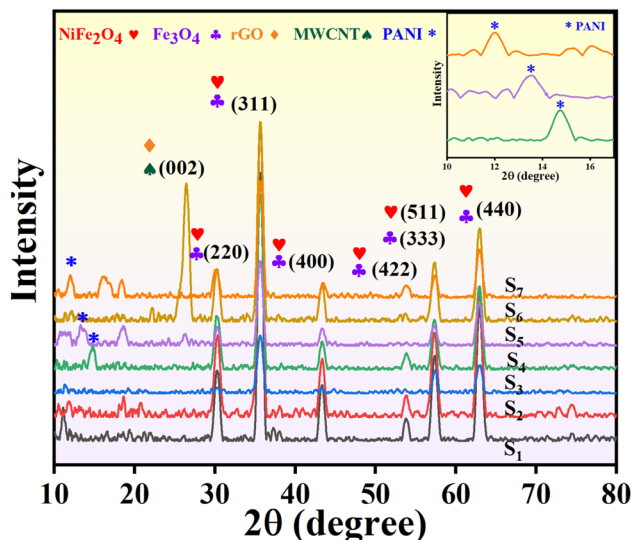


Fig. 2 XRD patterns of the synthesized nanocomposites: ( $\text{S}_1$ )  $\text{NiFe}_2\text{O}_4$ , ( $\text{S}_2$ )  $\text{NiFe}_2\text{O}_4/\text{Fe}_3\text{O}_4$ , ( $\text{S}_3$ )  $\text{NiFe}_2\text{O}_4/\text{Fe}_3\text{O}_4/\text{PANI}$ , ( $\text{S}_4$ )  $\text{NiFe}_2\text{O}_4/\text{Fe}_3\text{O}_4/\text{PANI}/\text{RGO}$ , ( $\text{S}_5$ )  $\text{NiFe}_2\text{O}_4/\text{Fe}_3\text{O}_4/\text{PANI}/\text{MWCNT}$ , ( $\text{S}_6$ )  $\text{NiFe}_2\text{O}_4/\text{Fe}_3\text{O}_4/\text{RGO}/\text{MWCNT}$ , ( $\text{S}_7$ )  $\text{NiFe}_2\text{O}_4/\text{Fe}_3\text{O}_4/\text{PANI}/\text{RGO}/\text{MWCNT}$ .

correspond to (111), (220), (311), (400), (422), (511), (440), and (533) crystal planes assigned to  $\text{Fe}_3\text{O}_4$ .

In the XRD pattern of sample  $\text{S}_2$ , several peaks are observed at consistent angles, indicating that the cubic spinel structure of  $\text{NiFe}_2\text{O}_4$  remains unchanged by the addition of  $\text{Fe}_3\text{O}_4$ . In the

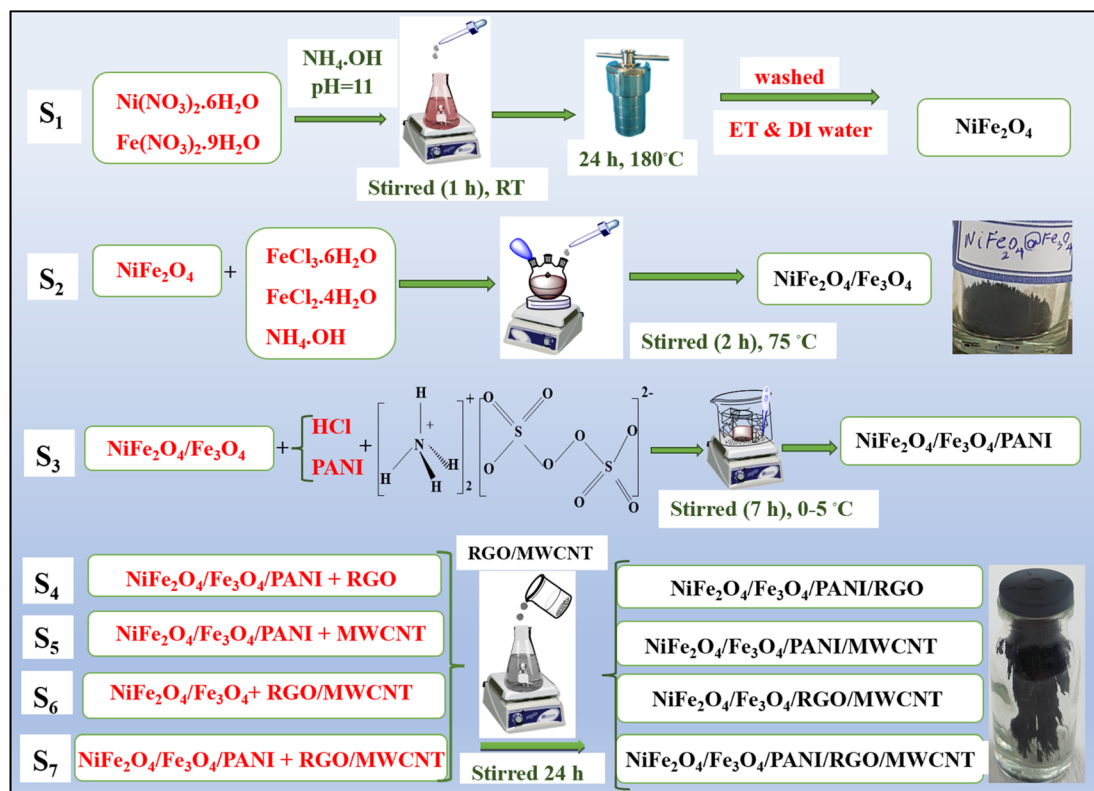


Fig. 1 Schematic representation of the synthesis of samples  $\text{S}_1$ ,  $\text{S}_2$ ,  $\text{S}_3$ ,  $\text{S}_4$ ,  $\text{S}_5$ ,  $\text{S}_6$ , and  $\text{S}_7$  at room temperature (RT).

XRD pattern of samples  $S_4$ ,  $S_5$ , and  $S_7$  (inset of Fig. 2), a weak peak at approximately  $2\theta = 14.7^\circ$ ,  $13.5^\circ$ ,  $12^\circ$  with low intensity corresponds to PANI.<sup>30,31</sup> The reduced intensity of the PANI peaks in sample  $S_3$  is probably attributed to its lower concentration within the composites.<sup>32</sup> The lack of a peak at  $2\theta = 26^\circ$ , typically associated with graphite, suggests that the presence of  $\text{NiFe}_2\text{O}_4$ ,  $\text{Fe}_3\text{O}_4$ , and PANI could potentially disrupt the layered structure of RGO. The robust bonding between these nanoparticles and RGO inhibits the rearrangement of RGO layers, resulting in the isolation of RGO layers.<sup>33,34</sup> The MWCNT-related peak in the XRD pattern of sample  $S_5$  is likely obscured due to the low MWCNT content in the composite.<sup>35</sup> In sample  $S_6$ , new peaks are observed at specified Bragg angles, with one prominent peak at  $26.6^\circ$ . This peak may be attributed to both RGO and MWCNT, as they typically exhibit diffraction peaks around  $26^\circ$  on the (002) plane. The presence of PANI in the samples causes a reduction in the intensity of the original peaks, as PANI absorbs some of the incident X-ray radiation.<sup>36</sup>

The crystallite sizes of the ferrite nanoparticles, calculated using Scherer's eqn (1), are indicated beside each graph.

$$\langle D \rangle = \frac{K \lambda}{\beta \cos \theta} \quad (1)$$

where  $\langle D \rangle$  represents the average diameter of the nanoparticles,  $\lambda$  is the X-ray wavelength,  $K$  is a dimensionless factor typically close to unity,  $\beta$  is the full width at half maximum of the diffraction peak, and  $\theta$  is the Bragg angle. According to Scherer's equation, the average nanoparticle sizes of the pure  $S_1$  and  $S_2$  samples were calculated to be 19.5 nm and 19 nm, respectively, showing a close similarity in size. The particle sizes of  $S_4$ ,  $S_5$ ,  $S_6$ , and  $S_7$  were determined to be 15.6 nm, 16.4 nm, 16.1 nm, and 15.2 nm, respectively. These measurements align well with the sizes observed in the SEM images.

Raman spectroscopy is a highly effective non-destructive technique used to characterize carbon materials and assess the degree of graphitization of carbon atoms in synthesized nanocomposites. The degree of crystallinity and presence of disorders/defects in carbon-based materials can be determined

by analyzing the intensity ratio of the D-band to the G-band.<sup>37</sup> To further elucidate the contributions of PANI, RGO, and MWCNT in the synthesized nanocomposites, Raman spectroscopy was employed using a 785 nm wavelength excitation laser. The Raman spectra of four prepared samples ( $S_4$ ,  $S_5$ ,  $S_6$ ,  $S_7$ ) are presented in Fig. 3.

In Fig. 3b, D- and G-bands centered at 1330 and 1585  $\text{cm}^{-1}$  for  $S_4$  show a red shift compared to free-standing RGO. The D-band arises from lattice defects in the carbon atoms, with higher defect concentrations correlating to increased D-band intensity. This band is linked to the vibrational modes of carbon atoms in the presence of structural defects that can perturb the  $\text{sp}^2$  hybridization network, resulting in enhanced phonon scattering.

On the other hand, the G-band primarily originates from the in-plane stretching vibration of carbon atoms in the  $\text{sp}^2$  hybridization of graphitic materials (degenerate in-plane  $\text{E}_{2g}$  mode of  $\text{sp}^2$  rings and chains at the  $\Gamma$  point). The 2D band is associated with the second-order Raman mode (degenerate in-plane  $\text{A}_{1g}$  breathing mode in rings at the K point).<sup>38,39</sup> Raman spectroscopic analysis of pristine MWCNT in the 500  $\text{cm}^{-1}$  to 1700  $\text{cm}^{-1}$  range revealed the presence of the D-band (around 1300  $\text{cm}^{-1}$ ), and the G-band (around 1600  $\text{cm}^{-1}$ ).<sup>40</sup> The observed Raman shifts for pure RGO are consistent with these values, with some polyaniline Raman peaks (e.g., around 1340 and 1585  $\text{cm}^{-1}$ ) showing similarities to the peaks of RGO and MWCNT. The presence of vibration modes in PANI, RGO, and MWCNT within the  $S_7$  nanocomposite (orange curve) leads to peak broadening, indicating the formation of new covalent bonds.<sup>34</sup> The integrated peaks, particularly around the D- and G-bands in  $S_7$ , signify significant contributions from each component. The broadband peaks incorporate contributions from PANI, MWCNT, and RGO in a symmetrical manner, resulting in a complex structure in  $S_7$  that highlights the heterogeneity of the nanocomposite samples.<sup>41,42</sup> The slight displacements of the D- and G-bands in the tested samples are attributed to their interactions with other components of the

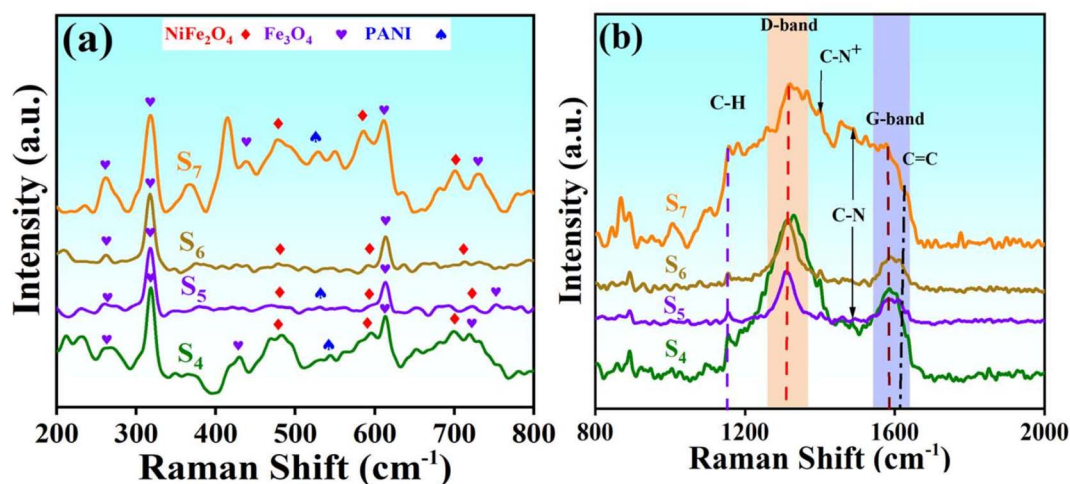


Fig. 3 Raman spectrum obtained for  $S_4$ ,  $S_5$ ,  $S_6$ , and  $S_7$  in different ranges from (a): (200–800  $\text{cm}^{-1}$ ) and (b): (800–2000  $\text{cm}^{-1}$ ).

nanocomposites. The peak intensities provide insights into the concentration of cations in each sample.<sup>41</sup> Additionally, there are broad, weak peaks around 2600–2700  $\text{cm}^{-1}$  corresponding to the 2D band.

Additional PANI peaks are illustrated in Fig. 3a. The C–H bond, arising from the bending vibration of the quinoid/benzenoid ring, is observed at 1155  $\text{cm}^{-1}$ . Additionally, the C–N stretching vibration bond associated with the benzenoid ring is detected at 1489  $\text{cm}^{-1}$  for  $S_7$ , 1486  $\text{cm}^{-1}$  for  $S_4$ , and 1492  $\text{cm}^{-1}$  for  $S_5$ . Raman spectra of all nanocomposite samples exhibit peaks attributed to  $\text{NiFe}_2\text{O}_4$  and  $\text{Fe}_3\text{O}_4$  in the 200–800  $\text{cm}^{-1}$  range, with slight displacements due to the varying composition of materials. The combined peaks are depicted in Fig. 3a and appear relatively weaker compared to the peaks related to the carbon-based materials in our nanocomposites. This disparity becomes apparent when materials are combined in a 1 : 1 mass ratio to create nanocomposites, as the volume of nickel ferrite is smaller than that of RGO and MWCNT. Consequently, detecting the presence of nickel ferrite within the overall nanocomposites using Raman spectroscopy can pose a challenge.<sup>38</sup>

Spinel ferrites typically exhibit 5 peaks in the 150–750  $\text{cm}^{-1}$  range, representing  $A_{1g}$ ,  $E_g$ , and three  $T_{2g}$  vibration modes. Some of these modes share similar characteristics between  $\text{NiFe}_2\text{O}_4$  and  $\text{Fe}_3\text{O}_4$ .<sup>41</sup> The  $I_D/I_G$  ratio is a key indicator of the level of graphitization in such materials. Enhancing the degree of graphitization is crucial for improving the electrical conductivity of the nanocomposites.<sup>37</sup>

Fourier transform infrared (FTIR) spectroscopy has been utilized to analyze the presence of various functional groups in nanocomposites and identify the types of bonds.<sup>14</sup> The FTIR spectra for the  $S_1$ ,  $S_2$ ,  $S_3$ ,  $S_4$ ,  $S_5$ ,  $S_6$ , and  $S_7$  samples in the wavenumber range of 3600–400  $\text{cm}^{-1}$  are shown in Fig. 4. The peak observed at 3427  $\text{cm}^{-1}$  is associated with the stretching

vibration bond of the hydroxyl (O–H covalent bond), indicating the adsorption of water on the surface of the nanocomposites. The appearance of characteristic peaks at 596  $\text{cm}^{-1}$ , and 667  $\text{cm}^{-1}$  correspond to metal–oxygen bonds Ni–O and Fe–O in all samples, suggesting the presence of an inverse spinel structure in the nanomagnetic composites and the uniform formation of  $\text{NiFe}_2\text{O}_4$  nanoparticles within the composite. Peaks at 1251  $\text{cm}^{-1}$  and 1119  $\text{cm}^{-1}$  are attributed to the stretching vibrations in the secondary amine C–N bond and the N=Q=N ring in the polyaniline structure. The absorption band at 1602  $\text{cm}^{-1}$  is assigned to the C=C bonds, while the narrow band at 2920  $\text{cm}^{-1}$  is determined by the stretching vibration of the C–H bond.

The morphology, particle size, and characterization analysis of the specimens were determined using SEM and TEM images, as depicted in Fig. 5 and 6. The SEM images are presented in Fig. 5a, and the corresponding EDS diagrams are shown in Fig. 5b. In Fig. 5 ( $S_2$ (a)), it can be observed that nanomagnetic particles of  $S_2$  have agglomerated in certain areas due to their magnetic properties. The EDS analysis of this specimen reveals the presence of Fe, O, and Ni elements (Fig. 5  $S_2$ (b)). The PANI networks formed after the polymerization process are decorated on  $\text{NiFe}_2\text{O}_4$  and  $\text{Fe}_3\text{O}_4$  (Fig. 5  $S_3$ (a)),<sup>43</sup> with the EDS diagram (Fig. 5  $S_3$ (a)) indicating the presence of N and C elements in addition to the previously mentioned elements in the nanocomposite structure. In Fig. 5 ( $S_4$ (a)), nanoparticles including ferrite nickel, the magnetic materials, and PANI are distributed nearly uniformly on the surface of the RGO sheet. Fig. 5 ( $S_5$ (a)) shows abundant nanoparticles are observed that adhere to the surface of carbon nanotubes. The EDS diagrams confirm the constituent elements of the nanocomposites. Fig. 5 ( $S_6$ (a,b)) illustrates the SEM and EDS of  $S_6$ —the absence of PANI, and the lack of nitrogen elements in the EDS analysis. Fig. 5 ( $S_7$ (a)) shows nanoparticles of  $\text{NiFe}_2\text{O}_4$ ,  $\text{Fe}_3\text{O}_4$ , PANI, and MWCNTs situated on the surface of RGO sheets. The EDS analysis reveals the presence of Ni, O, Fe, C, and N elements in the composition.

Fig. 6a–j displays the TEM images of the  $S_7$  sample, revealing the heterogeneous structure of the specimen. The series of images from (a) to (i) in Fig. 6 are sequentially magnified. In Fig. 6c and d, spherical core–shells of  $\text{NiFe}_2\text{O}_4$ @ $\text{Fe}_3\text{O}_4$  are evident. The dark regions represent the cores of  $\text{NiFe}_2\text{O}_4$  particles with high electron density, while the lighter areas surrounding the cores correspond to the  $\text{Fe}_3\text{O}_4$  shells. This contrast arises from variations in electron dispersion during transmission electron microscopy imaging. In Fig. 6d, it can be observed that the large surface area of RGO facilitates the uniform distribution of nanoparticles, which are to the OH groups of RGO and the OH groups of  $\text{NiFe}_2\text{O}_4$  particles.<sup>26</sup> As shown in Fig. 6c and e congress-like polymer chains of PANI are observed alongside some edges of nanotubes and around certain particle ferrites. This phenomenon is a result of the interaction between the oxygen atoms of ferrite and PANI. One of the primary reasons for incorporating PANI into nanocomposites is to prevent the aggregation of nanoparticles and facilitate their dispersion more effectively.<sup>31</sup> PANI serves as a protective layer around  $\text{NiFe}_2\text{O}_4$ / $\text{Fe}_3\text{O}_4$  particles. The average width of PANI nanospheres, which sometimes exhibit a rice

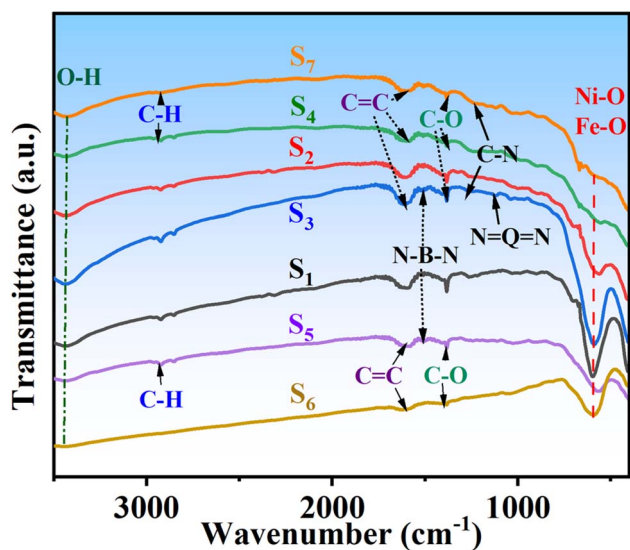


Fig. 4 FTIR analysis of ( $S_1$ )  $\text{NiFe}_2\text{O}_4$ , ( $S_2$ )  $\text{NiFe}_2\text{O}_4/\text{Fe}_3\text{O}_4$ , ( $S_3$ )  $\text{NiFe}_2\text{O}_4/\text{Fe}_3\text{O}_4/\text{PANI}$ , ( $S_4$ )  $\text{NiFe}_2\text{O}_4/\text{Fe}_3\text{O}_4/\text{PANI}/\text{RGO}$ , ( $S_5$ )  $\text{NiFe}_2\text{O}_4/\text{Fe}_3\text{O}_4/\text{PANI}/\text{MWCNT}$ , ( $S_6$ )  $\text{NiFe}_2\text{O}_4/\text{Fe}_3\text{O}_4/\text{MWCNT}/\text{RGO}$ , ( $S_7$ )  $\text{NiFe}_2\text{O}_4/\text{Fe}_3\text{O}_4/\text{PANI}/\text{RGO}/\text{MWCNT}$  samples.

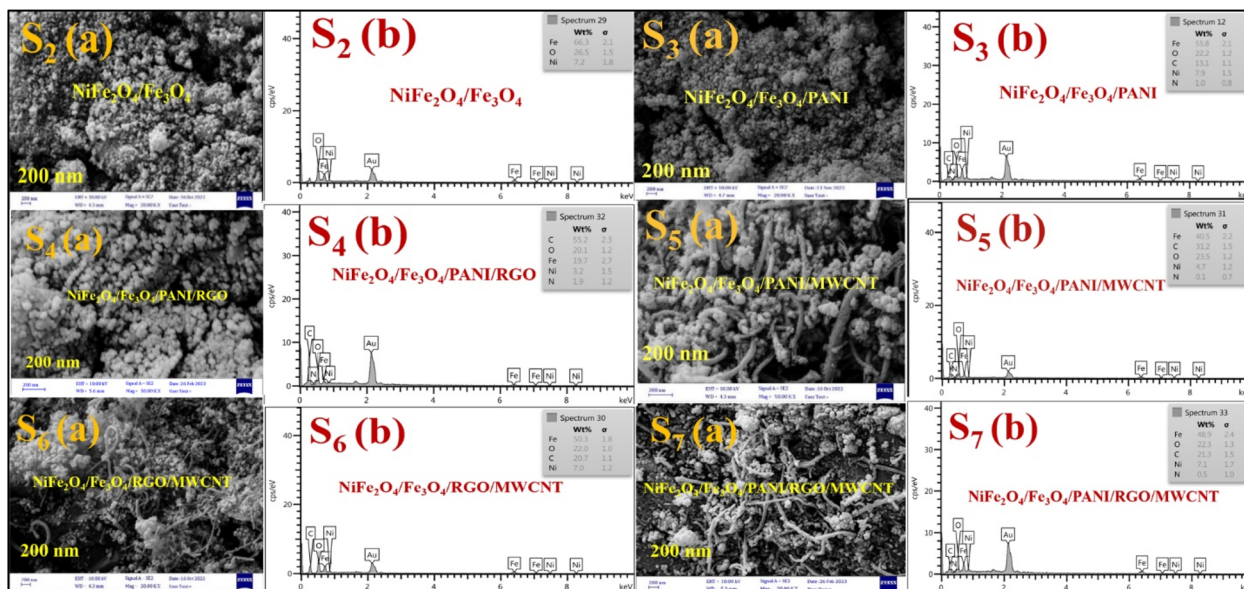


Fig. 5 SEM images and EDS analysis of  $S_1(a,b)$ ,  $S_2(a,b)$ ,  $S_3(a,b)$ ,  $S_4(a,b)$ ,  $S_5(a,b)$ ,  $S_6(a,b)$ ,  $S_7(a,b)$ .  $NiFe_2O_4/Fe_3O_4$  ( $S_2$ ),  $NiFe_2O_4/Fe_3O_4/PANI$  ( $S_3$ ),  $NiFe_2O_4/Fe_3O_4/PANI/RGO$  ( $S_4$ ),  $NiFe_2O_4/Fe_3O_4/PANI/MWCNT$  ( $S_5$ ),  $NiFe_2O_4/Fe_3O_4/MWCNT/RGO$  ( $S_6$ ),  $NiFe_2O_4/Fe_3O_4/PANI/RGO/MWCNT$  ( $S_7$ ) samples.

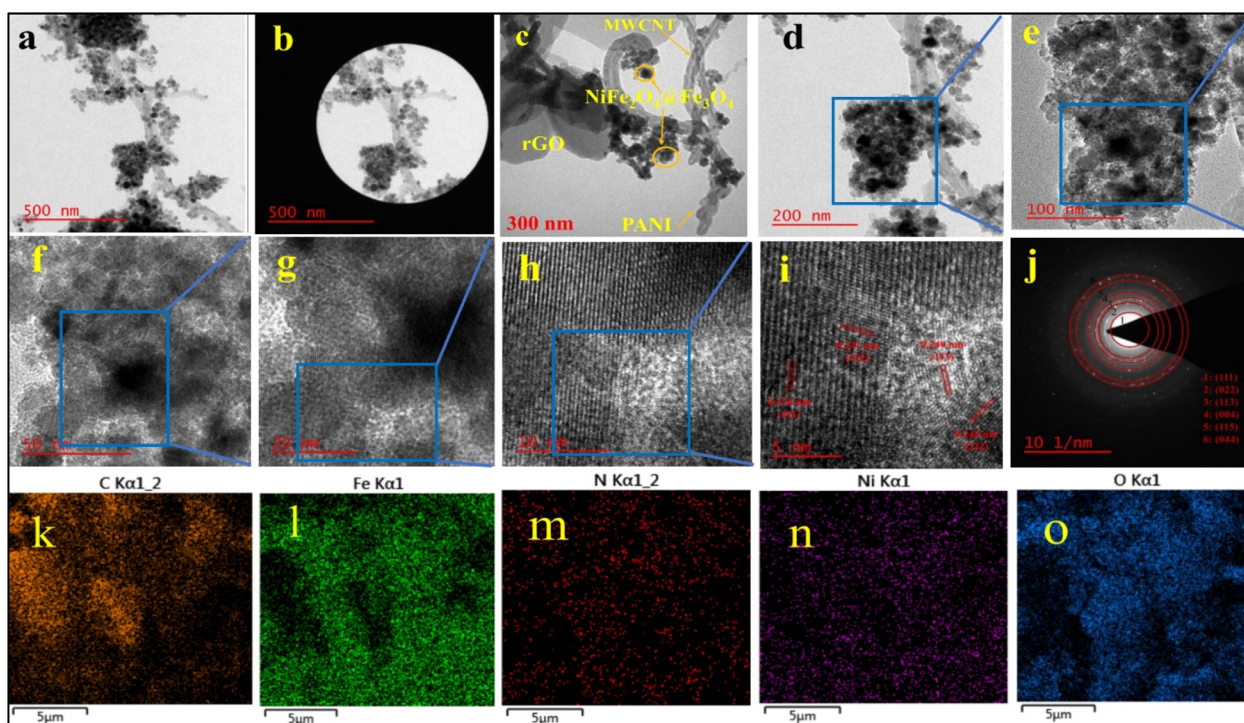


Fig. 6 TEM images of  $S_7$  ( $NiFe_2O_4/Fe_3O_4/PANI/RGO/MWCNT$ ) in different scales: (a and b) 500 nm, (c) 300 nm, (d) 200 nm, (e) 100 nm, (f) 50 nm, (g) 20 nm, (h) 10 nm, (i) 5 nm, (j) SAED and (k–o) EDS elemental mapping.

grain shape, ranges from 42 to 129 nm. The median size of the  $NiFe_2O_4/Fe_3O_4$  composite falls between 17.8 and 37.9 nm, aligning with the sizes calculated using the Debye–Scherrer equation. The TEM images validate the findings from the SEM images, confirming the successful synthesis of the samples. In

Fig. 6k–o, the element mapping analysis of  $S_7$  demonstrates a uniform distribution of C, Fe, N, Ni, and O elements, indicating the successful synthesis of  $S_7$ . In HRTEM image (i), lattice spacing values of 0.476, 0.245, 0.241, and 0.249 correspond to (111), (222), (222), and (113) planes, respectively, matching the

*d*-spacing values obtained from XRD analysis of NiFe<sub>2</sub>O<sub>4</sub> and Fe<sub>3</sub>O<sub>4</sub>. These values are further corroborated by the *d*-spacing values derived from the SAED analysis.

### 3.1 Magnetic properties by VSM analysis

The magnetic characteristics of the nanocomposites were measured using a vibration sample magnetometer (VSM) device. As depicted in Fig. 7, the hysteresis diagram of the samples changes with the applied magnetic field in the range of −14 to 14 kOe. The inset of Fig. 7 highlights the presence of very

low hysteresis, indicating superparamagnetic behavior in the nanocomposites. The saturation magnetization of S<sub>1</sub>, S<sub>2</sub>, S<sub>3</sub>, S<sub>4</sub>, S<sub>5</sub>, S<sub>6</sub>, and S<sub>7</sub> are 35.18, 66.92, 21.83, 27.55, 26.31, 15.40, and 27.29 (emu g<sup>−1</sup>) respectively, at a maximum magnetic field of 14 kOe.

The addition of Fe<sub>3</sub>O<sub>4</sub> to Ni ferrite enhances saturation magnetization, while PANI decreases the magnetic property of S<sub>3</sub>.<sup>17</sup> Typically, the introduction of RGO results in a decrease in the saturation magnetization of the nanocomposites, although there exists an optimal value for this effect. Additionally, a specific amount of RGO can actually enhance magnetization to some extent.<sup>44</sup> The presence of MWCNT contributes to a decrease in the saturation magnetization (*M<sub>s</sub>*) of S<sub>5</sub>. In fact, both RGO and MWCNT contribute almost equally to the reduction in *M<sub>s</sub>*.<sup>45</sup> The total quantity of RGO and MWCNT utilized in S<sub>7</sub> is equivalent to the amount of RGO in S<sub>4</sub> or the amount of MWCNT in S<sub>5</sub>, leading to similar magnetization properties for these nanocomposites.

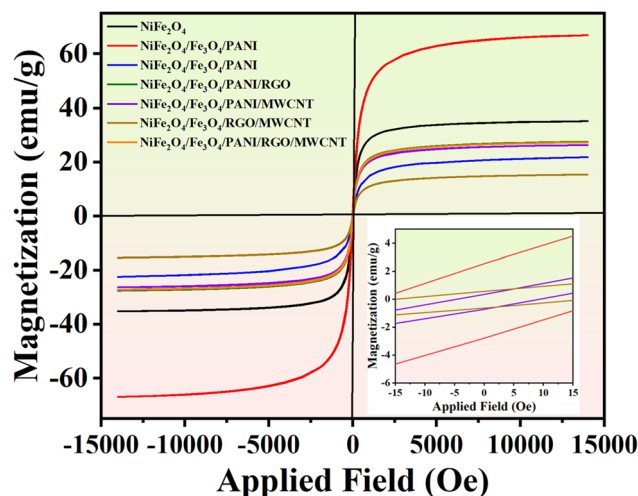


Fig. 7 VSM analysis of synthesized nanocomposites: (S<sub>1</sub>) NiFe<sub>2</sub>O<sub>4</sub>, (S<sub>2</sub>) NiFe<sub>2</sub>O<sub>4</sub>/Fe<sub>3</sub>O<sub>4</sub>, (S<sub>3</sub>) NiFe<sub>2</sub>O<sub>4</sub>/Fe<sub>3</sub>O<sub>4</sub>/PANI, (S<sub>4</sub>) NiFe<sub>2</sub>O<sub>4</sub>/Fe<sub>3</sub>O<sub>4</sub>/PANI/RGO, (S<sub>5</sub>) NiFe<sub>2</sub>O<sub>4</sub>/Fe<sub>3</sub>O<sub>4</sub>/PANI/MWCNT, (S<sub>6</sub>) NiFe<sub>2</sub>O<sub>4</sub>/Fe<sub>3</sub>O<sub>4</sub>/RGO/MWCNT, (S<sub>7</sub>) NiFe<sub>2</sub>O<sub>4</sub>/Fe<sub>3</sub>O<sub>4</sub>/PANI/RGO/MWCNT.

### 3.2 Microwave absorption analysis

To better understand the absorption mechanism of microwaves, the electromagnetic parameters were measured using a vector network analyzer.<sup>17</sup> The complex permittivity ( $\epsilon_r = \epsilon' - j\epsilon''$ ) and complex permeability ( $\mu_r = \mu' - j\mu''$ ) of the prepared nanocomposite demonstrate strong frequency-dependent properties. The real parts show the storage of electric and magnetic energy, while the imaginary parts indicate the dissipation capacity of electromagnetic energy.<sup>46</sup> Generally, the dielectric constant is mainly influenced by the material's conductivity. As shown in Fig. 8a, the  $\epsilon'$  of all nanocomposite samples tends to decrease, with samples without MWCNT

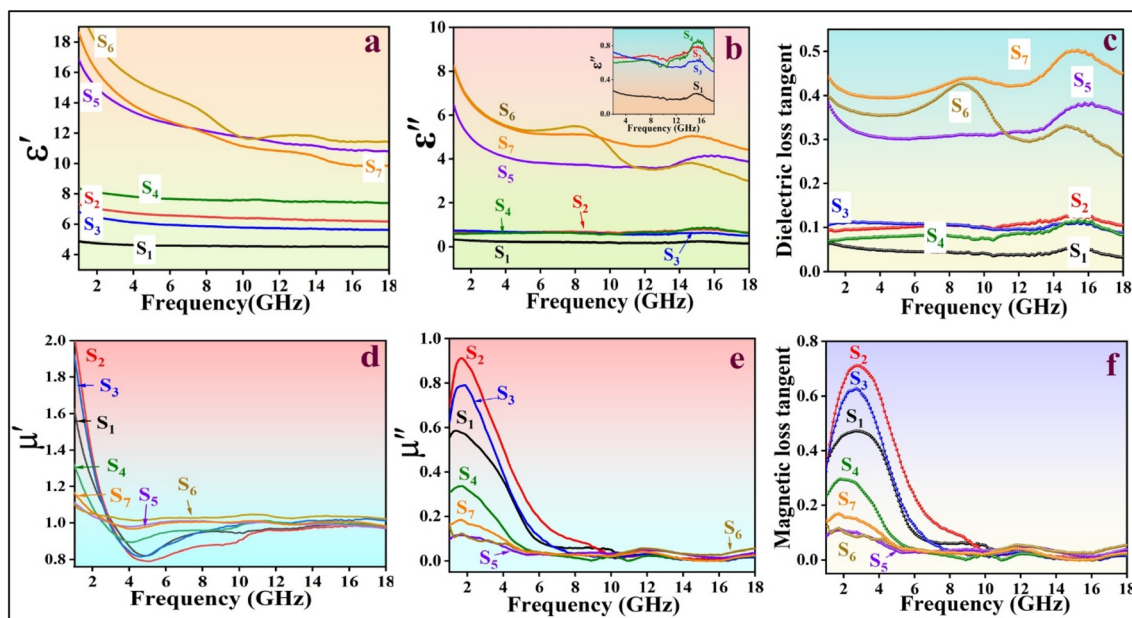


Fig. 8 (a and b) Real part ( $\epsilon'$ ), and imaginary part ( $\epsilon''$ ) of complex permittivity, (c) dielectric loss tangent, (d and e) real part ( $\mu'$ ) and imaginary part ( $\mu''$ ) of complex permeability, (f) magnetic loss tangent, respectively for: (S<sub>1</sub>) NiFe<sub>2</sub>O<sub>4</sub>, (S<sub>2</sub>) NiFe<sub>2</sub>O<sub>4</sub>/Fe<sub>3</sub>O<sub>4</sub>, (S<sub>3</sub>) NiFe<sub>2</sub>O<sub>4</sub>/Fe<sub>3</sub>O<sub>4</sub>/PANI, (S<sub>4</sub>) NiFe<sub>2</sub>O<sub>4</sub>/Fe<sub>3</sub>O<sub>4</sub>/PANI/RGO, (S<sub>5</sub>) NiFe<sub>2</sub>O<sub>4</sub>/Fe<sub>3</sub>O<sub>4</sub>/PANI/MWCNT, (S<sub>6</sub>) NiFe<sub>2</sub>O<sub>4</sub>/Fe<sub>3</sub>O<sub>4</sub>/RGO/MWCNT, (S<sub>7</sub>) NiFe<sub>2</sub>O<sub>4</sub>/Fe<sub>3</sub>O<sub>4</sub>/PANI/RGO/MWCNT.

showing a smaller reduction with frequency. This decrease is attributed to the frequency dispersion effect, where dipole directions align with the low-frequency electric field but cannot keep up with fluctuations in the high-frequency fields, leading to charge accumulation. Samples with MWCNT exhibit higher real permittivity, indicating their high storage electric capacity.<sup>45</sup> The presence of RGO in combination with MWCNT in  $S_6$ , leads to interfacial polarization between RGO and other components, causing charge accumulation within the interfaces.<sup>47</sup> In the case of  $S_7$ , PANI balances the magnetic and electric components with varying magnetic and dielectric properties, resulting in the low  $\epsilon'$  of  $S_7$ .<sup>17</sup> The addition of RGO to  $S_4$  resulted in an increased electric storage energy compared to the other samples, with the exception of those containing MWCNT. The high  $\epsilon'$  of the  $S_5$  and  $S_7$  not only results in high conductivity but also provides good impedance matching.<sup>48</sup> Due to the presence of PANI coating as a conductive polymer, RGO sheets, and MWCNT, the dielectric loss  $\epsilon''$  decreases with increasing frequency.<sup>49</sup> The dielectric loss of  $S_6$  is higher than other samples up to 9.3 GHz (Fig. 8b), then gradually decreases with two resonance peaks, indicating the presence of multi-polarization relaxation involving dipole and interfacial polarizations.<sup>50</sup> The dipole polarizations originate from defects in RGO sheets, MWCNT, and PANI, as well as functional groups such as oxygenated chemical bonds (C=O and C-O bonds) connected to PANI and RGO. The diverse electron capabilities of carbon and oxygen atoms cause electron movements that generate polarization under periodic electromagnetic fields.<sup>28</sup> Other polarization mechanisms arise from heterogeneous junctions, leading to interface polarization. The compositions of different magnetic and electric materials (NiFe<sub>2</sub>O<sub>4</sub>, Fe<sub>3</sub>O<sub>4</sub>, PANI, RGO, MWCNT) create a heterojunction structure that enhances the interfacial area by providing active chemical sites to connect functional groups in RGO and MWCNT.<sup>50</sup> According to free-space theory, higher  $\epsilon''$  indicates greater conductivity in samples containing MWCNT.<sup>51</sup> In  $S_6$ , a minor peak at 8.3 GHz is detected, attributed to significant polarization loss between MWCNT-RGO and the magnetic components, as well as between Fe, Ni, and the PANI coating.<sup>49</sup>

As depicted in Fig. 8d and e, the real part ( $\mu'$ ) and imaginary part ( $\mu''$ ) of all samples exhibit a similar decreasing trend. The formation of magnetic dipoles in nanocomposites is influenced by  $\mu'$ , particularly materials with unpaired electrons. The combination of Fe<sub>3</sub>O<sub>4</sub> with nickel ferrite enhances the magnetic storage capacity.<sup>52</sup> Initially, the NiFe<sub>2</sub>O<sub>4</sub>/Fe<sub>3</sub>O<sub>4</sub> composite shows the highest  $\mu'$  value at the lower end of the frequency range. Subsequently, the introduction of nonmagnetic materials leads to a decrease in  $\mu'$ . Samples containing MWCNT exhibit a slower decreasing trend in  $\mu'$  with frequency compared to other samples. As depicted in (Fig. 8e), with an increase in the amount of magnetic ingredients, there is a higher magnetic loss observed, making NiFe<sub>2</sub>O<sub>4</sub>/Fe<sub>3</sub>O<sub>4</sub> exhibit the greatest magnetic loss up to 10 GHz.

Superparamagnetic materials have electrons with unpaired spins that respond to periodic magnetic fields. At frequencies between 2–10 GHz, magnetic moments rotate more slowly compared to 10–18 GHz frequencies. The presence of more magnetic ingredients in a sample, results in more magnetic

moments, facilitating relaxation at low-frequency ranges. In high frequencies, numerous moments may not be able to follow the EM field fluctuations. The addition of nonmagnetic materials, such as MWCNT, reduces the number of magnetic moments and makes spin rotation relaxation easier, and consequently, the magnetic loss tangent ( $\mu''$ ) can contribute to maintaining a low and consistent magnetic loss tangent within the 10–18 GHz frequency range.

Negative values in the magnetic loss of  $S_4$  may occur in response to a periodic EM field. When a conductive composite is exposed to an external periodic magnetic field, an internal electrical field is generated, affecting the movement of charges within the nanocomposite and leading to induced magnetic fields. If the internal magnetic field surpasses the external magnetic field,  $\mu''$  can exhibit negative values.<sup>53</sup> In the frequency range of 2–10 GHz, the magnetic loss of samples containing nonmagnetic materials decreases, indicating natural resonance. However, in 10–18 GHz frequencies, the dominant loss mechanism is eddy currents with a minimal contribution from exchange resonance (Fig. 8e and f). There are additional magnetic loss mechanisms, such as domain wall resonance, that typically occur at lower frequencies (<100 MHz), which were not investigated in this study.

The high conductivity of MWCNT contributes to samples containing MWCNT having a higher dielectric loss tangent compared to other samples, while their magnetic loss tangent is lower. The dielectric loss tangent of  $S_7$  is the highest due to its three conductive components.

As depicted in Fig. 8c, the dielectric loss tangent curves of all specimens with MWCNT are higher compared to others, strengthening the dielectric loss capacity. The multi-component structure of  $S_7$  leads to the highest value of  $\tan \delta_\epsilon$ , primarily due to the interfacial polarization mechanism. However, some other important factors affected the MA and they will be discussed.

In Fig. 8f, the magnetic loss tangent of all samples tends to decrease with increasing frequency. The magnetic loss tangent of NiFe<sub>2</sub>O<sub>4</sub>/Fe<sub>3</sub>O<sub>4</sub> ( $S_2$ ) surpasses the others up to 9.1 GHz, demonstrating significant magnetic loss capabilities. A distinct peak associated with natural resonance is observed at lower frequencies.

The magnetic loss tangent remains stable between 10 GHz and 18 GHz across all samples. In samples containing PANI, like  $S_4$ , occasional negative values are observed at certain frequencies, possibly stemming from negative magnetic loss ( $\mu''$ ) values at those specific frequencies.<sup>54</sup> Furthermore, in the 10–18 GHz range, the dielectric loss tangent is notably higher than the magnetic loss tangent, particularly in samples containing MWCNT. This suggests a predominant dielectric loss mechanism within the specimens.<sup>54</sup>

Electromagnetic protective materials need to possess specific attributes, including lightweight, thinness, and a broad absorption bandwidth.<sup>55</sup> The reflection loss (RL) can assess these properties and is calculated using the transmission line theory (eqn (2)):

$$RL = 20 \log \left( \left| \frac{Z_{in} - 1}{Z_{in} + 1} \right| \right) \quad (2)$$

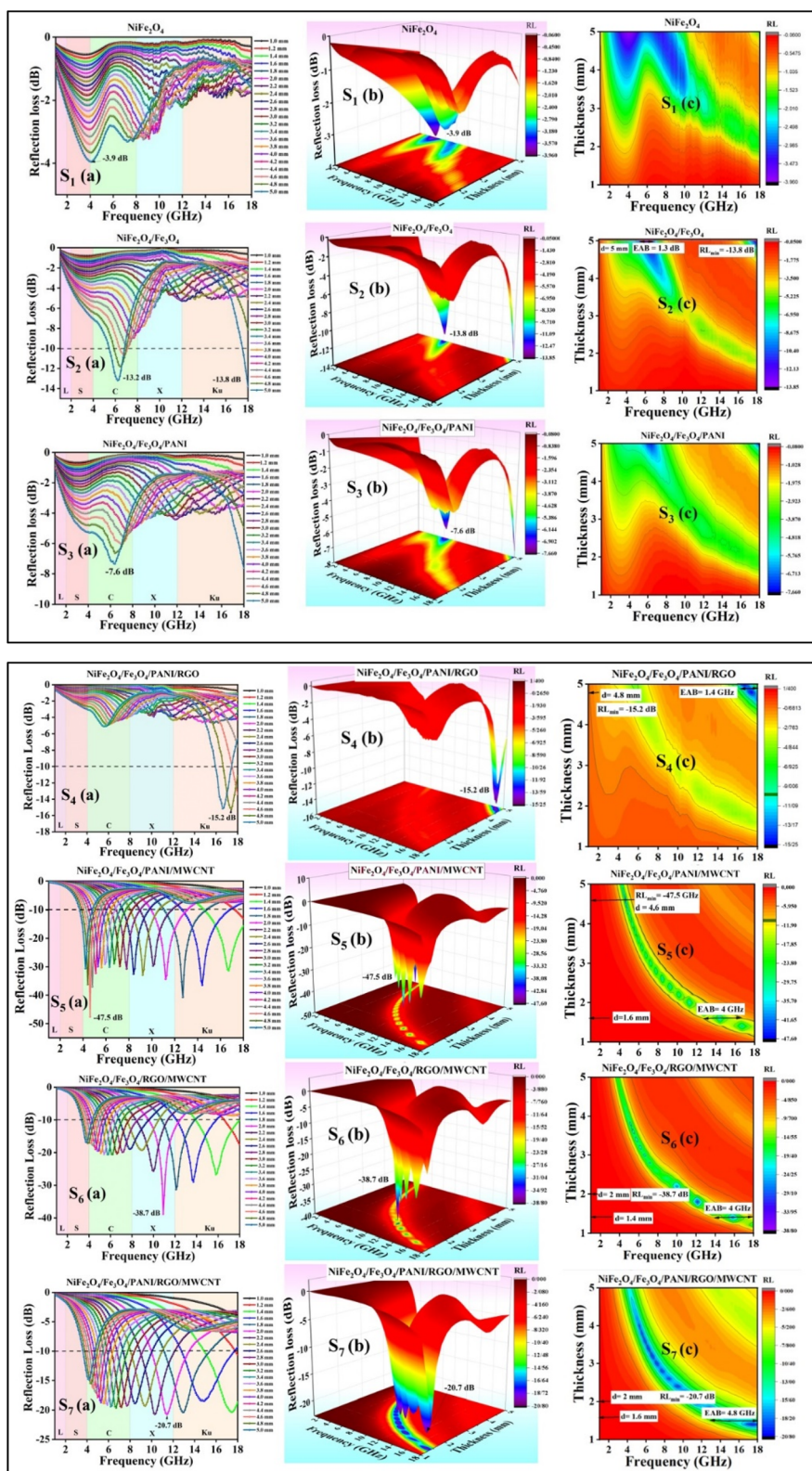


Fig. 9 (a) 2D, (b) 3D reflection loss diagrams and (c) contour diagram of thickness versus frequency for (S<sub>1</sub>) NiFe<sub>2</sub>O<sub>4</sub>, (S<sub>2</sub>) NiFe<sub>2</sub>O<sub>4</sub>/Fe<sub>3</sub>O<sub>4</sub>, (S<sub>3</sub>) NiFe<sub>2</sub>O<sub>4</sub>/Fe<sub>3</sub>O<sub>4</sub>/PANI, (S<sub>4</sub>) NiFe<sub>2</sub>O<sub>4</sub>/Fe<sub>3</sub>O<sub>4</sub>/PANI/RGO, (S<sub>5</sub>) NiFe<sub>2</sub>O<sub>4</sub>/Fe<sub>3</sub>O<sub>4</sub>/PANI/MWCNT, (S<sub>6</sub>) NiFe<sub>2</sub>O<sub>4</sub>/Fe<sub>3</sub>O<sub>4</sub>/RGO/MWCNT, and (S<sub>7</sub>) NiFe<sub>2</sub>O<sub>4</sub>/Fe<sub>3</sub>O<sub>4</sub>/PANI/RGO/MWCNT.

The RL can be calculated from  $\epsilon_r$  and  $\mu_r$  quantities. The input impedance is defined by eqn (3):<sup>56</sup>

$$Z_{in} = Z_0 \sqrt{\frac{\mu_r}{\epsilon_r}} \tanh \left[ j \left( \frac{2\pi}{c} \right) f d \sqrt{\mu_r \epsilon_r} \right] \quad (3)$$

where the impedance of free space, denoted as  $Z_0$ , the frequency, denoted as  $f$ , and the layer thickness of the sample, denoted as  $d$ , are important parameters in the analysis.

Fig. 9 depicts the planar diagrams, 3D RL, 2D RL, and the contour map at different thicknesses for all the prepared nanocomposites. The 3D RL diagrams vary based on the material thickness (ranging from 1.0 to 5.0 mm) and microwave frequency (2–18 GHz), aligning with the 2D RL diagrams. The intensities of RL are indicated by varying colors in both the 3D and contour RL diagrams.

The effective absorption bandwidth (EAB) is a crucial parameter for the microwave absorption of the specimens. It signifies the frequency range where the RL values are below  $-10$  dB.<sup>57</sup> This implies that if  $RL < -10$  dB, the sample will absorb over 90% of the incident EM waves.<sup>58</sup> In Fig. 9  $S_1$ (a–c), despite having moderate magnetic loss, the RL values of the  $NiFe_2O_4$  sample indicate poor MA performance, with  $RL_{min}$  values exceeding  $-10$  dB within 2–18 GHz. Therefore, this sample should be combined with other materials. Magnetite can significantly enhance the absorption properties of the nanocomposites due to its high magnetic properties. In Fig. 9  $S_2$ (a–c),  $S_2$  exhibits  $RL_{min} = -13.8$  dB at 18 GHz, with an EAB of 1.3 GHz at  $d = 5$  mm. Fig. 9  $S_4$ (a–c) illustrates  $S_4$  with  $RL_{min} = -15.2$  dB at 17.4 GHz ( $d = 4.8$  mm). The RGO sheets somewhat enhance the conductivity characteristics of the previous sample, with an EAB of 1.4 GHz.  $S_5$  exhibits the highest  $RL_{min}$  value of  $-47.5$  dB at 4.6 GHz ( $d = 4.6$  mm) among all samples, with an EAB of 4 GHz at  $d = 1.6$  mm (Fig. 9  $S_5$ (a–c)). The introduction of MWCNT

to the composite has led to an improvement in MA performance.

Analysis from Fig. 9  $S_6$ (a–c) shows that  $S_6$  not only demonstrates good EAB and microwave absorption compared to previous samples but also achieves an  $RL_{min}$  of  $-38.7$  dB at 10.9 GHz for a thickness of 2 mm, with the EAB remaining at 4 GHz within the range of 14–18 GHz. The broadest EAB among all samples belongs to  $S_7$ , which is 4.8 GHz at  $d = 1.6$  mm.  $RL_{min}$  is  $-20.7$  dB at 11.4 GHz ( $d = 2$  mm) for  $S_7$ . It is worth noting that for samples  $S_5$ ,  $S_6$ , and  $S_7$ , nearly all  $RL_{min}$  values for various thicknesses are below  $-10$  dB, demonstrating the strong microwave absorption capabilities of the samples. In  $S_7$ , the synergic effects of RGO, MWCNT, and PANI in producing an extended conductive network have led to this phenomenon and expanded the EAB to 4.8 GHz, the widest EAB among all samples. The thickness of the absorbent material greatly influences the MA performance. The last two samples ( $S_6$  and  $S_7$ ) exhibit fantastic MA properties at thin thickness ( $d = 2$  mm) (Fig. 10).

Table 1 displays the  $RL_{min}$ , absorber thickness, EAB, coercive field ( $H_c$ ), remanence magnetization ( $M_r$ ), and saturation magnetization ( $M_s$ ) of all the prepared samples.

In Fig. 11a and b, the 3D and 2D reflection loss *versus* frequency is depicted. Fig. 11c illustrates a radar chart for  $S_2$ ,  $S_4$ ,  $S_5$ ,  $S_6$ , and  $S_7$ , showing their thickness, filler content, and EAB. Additionally, Fig. 11d displays the EAB for  $S_2$ ,  $S_4$ ,  $S_5$ ,  $S_6$ , and  $S_7$ .

Fig. 12 compares the absorption parameters of our work with some related studies, including  $RL_{min}$ , EAB, and absorption thickness.

While the RL parameter is essential for describing the microwave absorption (MA) performance of materials, impedance matching is also crucial. Impedance matching plays a key

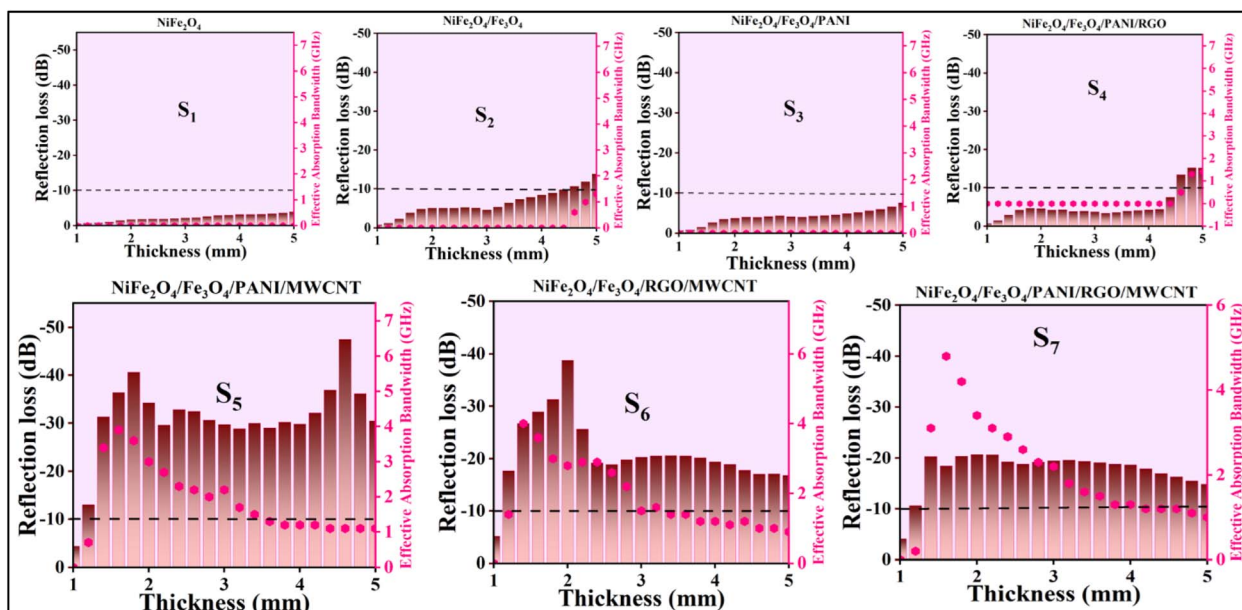
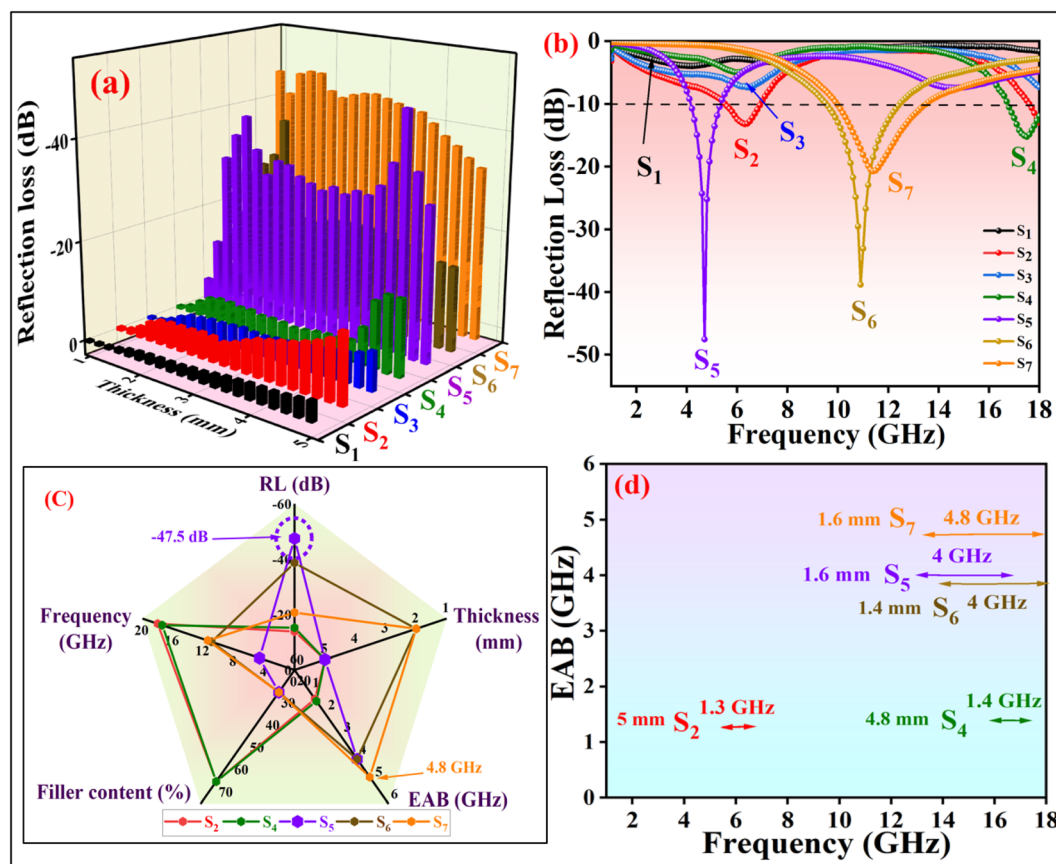


Fig. 10 RL and EAB *versus* thickness for ( $S_1$ )  $NiFe_2O_4$ , ( $S_2$ )  $NiFe_2O_4/Fe_3O_4$ , ( $S_3$ )  $NiFe_2O_4/Fe_3O_4/PANI$ , ( $S_4$ )  $NiFe_2O_4/Fe_3O_4/PANI/RGO$ , ( $S_5$ )  $NiFe_2O_4/Fe_3O_4/PANI/MWCNT$ , ( $S_6$ )  $NiFe_2O_4/Fe_3O_4/RGO/MWCNT$ , ( $S_7$ )  $NiFe_2O_4/Fe_3O_4/PANI/RGO/MWCNT$ .

**Table 1**  $RL_{\min}$ , frequency, absorber thickness, EAB,  $H_c$ ,  $M_r$ ,  $M_s$  of  $S_1$ ,  $S_2$ ,  $S_3$ ,  $S_4$ ,  $S_5$ ,  $S_6$ , and  $S_7$ 

Sample	RLmin (dB)	$f$ (GHz)	$t_m$ (mm)	EAB (GHz)	$ H_c $ (Oe)	$M_r$ (emu g <sup>-1</sup> )	$M_s$ (emu g <sup>-1</sup> )
NiFe <sub>2</sub> O <sub>4</sub> ( $S_1$ )	-3.9	4.1	5	0	23.4	2.5	35.18
NiFe <sub>2</sub> O <sub>4</sub> /Fe <sub>3</sub> O <sub>4</sub> ( $S_2$ )	-13.8	18	5	1.3	17.9	2.6	66.92
NiFe <sub>2</sub> O <sub>4</sub> /Fe <sub>3</sub> O <sub>4</sub> /PANI ( $S_3$ )	-7.6	18	5	0	7.8	0.36	21.8
NiFe <sub>2</sub> O <sub>4</sub> /Fe <sub>3</sub> O <sub>4</sub> /PANI/RGO ( $S_4$ )	-15.2	17.4	4.8	1.4	3.8	0.31	27.55
NiFe <sub>2</sub> O <sub>4</sub> /Fe <sub>3</sub> O <sub>4</sub> /PANI/MWCNT ( $S_5$ )	-47.5	4.6	4.6	4	4.7	0.35	26.31
NiFe <sub>2</sub> O <sub>4</sub> /Fe <sub>3</sub> O <sub>4</sub> /RGO/MWCNT ( $S_6$ )	-38.7	10.9	2	4	14.6	0.57	15.40
NiFe <sub>2</sub> O <sub>4</sub> /Fe <sub>3</sub> O <sub>4</sub> /PANI/RGO/MWCNT ( $S_7$ )	-20.7	11.4	2	4.8	7.4	0.58	27.29

**Fig. 11** (a) Reflection loss of all samples, (b) the best  $RL_{\min}$ , (c) radar chart, (d) EAB for: ( $S_1$ ) NiFe<sub>2</sub>O<sub>4</sub>, ( $S_2$ ) NiFe<sub>2</sub>O<sub>4</sub>/Fe<sub>3</sub>O<sub>4</sub>, ( $S_3$ ) NiFe<sub>2</sub>O<sub>4</sub>/Fe<sub>3</sub>O<sub>4</sub>/PANI, ( $S_4$ ) NiFe<sub>2</sub>O<sub>4</sub>/Fe<sub>3</sub>O<sub>4</sub>/PANI/RGO, ( $S_5$ ) NiFe<sub>2</sub>O<sub>4</sub>/Fe<sub>3</sub>O<sub>4</sub>/PANI/MWCNT, ( $S_6$ ) NiFe<sub>2</sub>O<sub>4</sub>/Fe<sub>3</sub>O<sub>4</sub>/RGO/MWCNT, ( $S_7$ ) NiFe<sub>2</sub>O<sub>4</sub>/Fe<sub>3</sub>O<sub>4</sub>/PANI/RGO/MWCNT.

role in the absorption of electromagnetic waves and is defined in eqn (4)

$$\left| \frac{Z_{in}}{Z_0} \right| = 1 \quad (4)$$

When the impedance matching value is close to 1, the absorbing material can absorb EM waves effectively without reflection.<sup>59</sup> Fig. 13 shows that the impedance matching values of samples containing MWCNT ( $S_5$ ,  $S_6$ ,  $S_7$ ) are nearly equal to 1 compared to samples without MWCNT. Despite the higher dielectric loss of  $S_7$  compared to  $S_6$  and  $S_5$ ,  $S_5$  demonstrates the best  $RL_{\min}$  due to its superior impedance-matching capabilities.

In Fig. 13c, the impedance matching of all samples *versus* frequency is depicted for the thicknesses that include the best  $RL_{\min}$ .

The input impedance matching coefficient ( $M_z$ ), defined in eqn (5), is shown only for the best values of each sample in Fig. 13d and detail for all samples in Fig. 14:

$$M_z = \frac{2Z'_{in}}{|Z_{in}|^2 + 1} \quad (5)$$

where,  $Z'_{in}$  is the real normalized input impedance. If the characteristic impedance of the material is nearly equivalent to the characteristic impedance of free space, ( $M_z$ ) impedance matching is close to 1, and therefore this good impedance

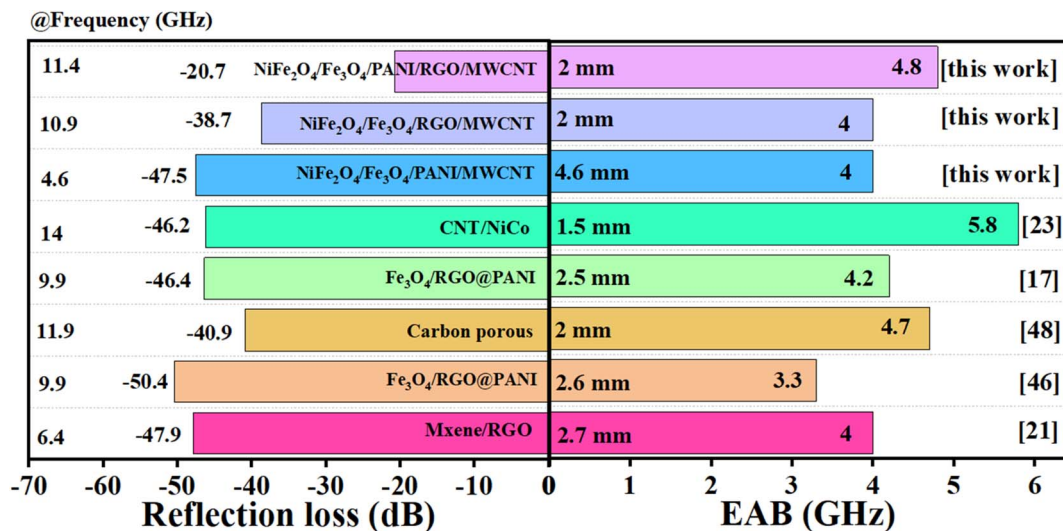


Fig. 12 The comparison of absorption parameters of our work with other related studies.

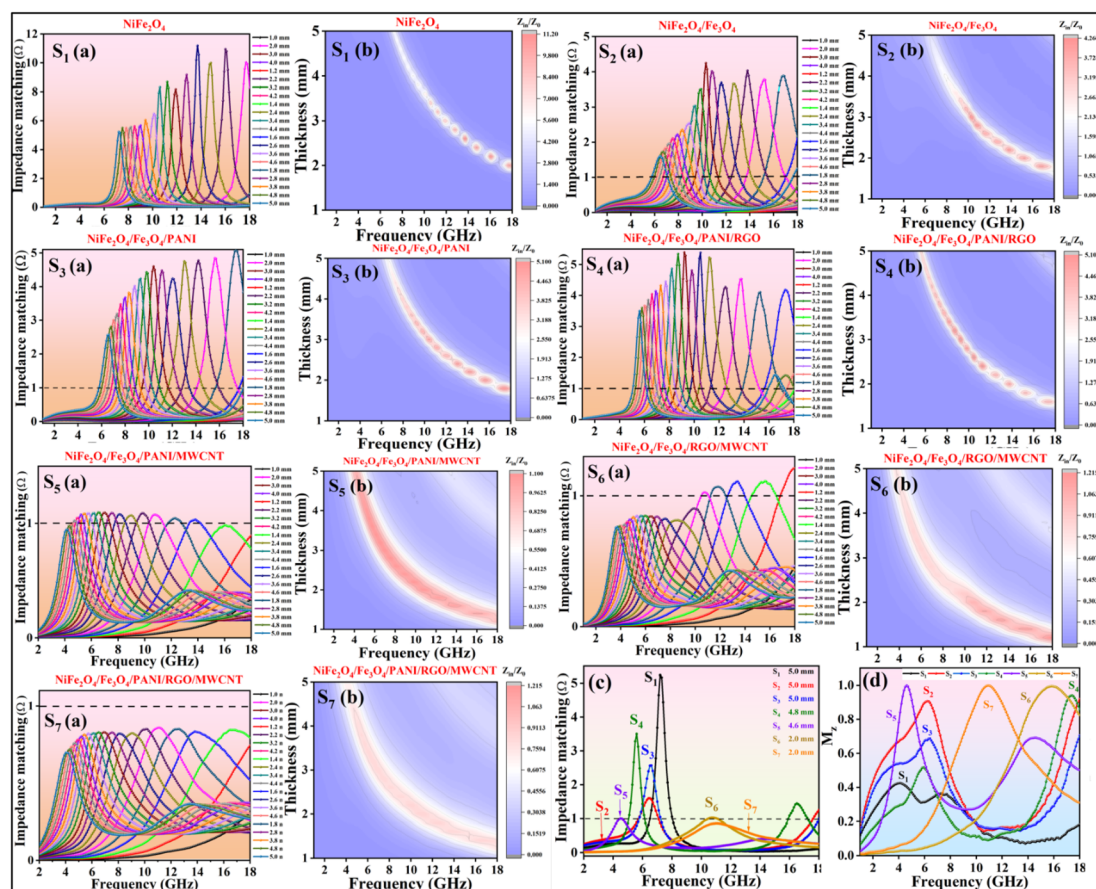


Fig. 13 2D (a), contour impedance matching diagrams (b), the  $Z$  (impedance matching) versus frequency for thickness including the best  $RL_{min}$  (c), the best input impedance matching coefficient ( $M_z$ ) (d) of  $S_1$ ,  $S_2$ ,  $S_3$ ,  $S_4$ ,  $S_5$ ,  $S_6$ ,  $S_7$ .

matching causes to strengthened absorption peak.<sup>60</sup> Fig. 14 illustrates that compared to the other samples,  $S_5$ ,  $S_6$ , and  $S_7$  have acceptable  $M_z$  values, indicating their good impedance matching and high electromagnetic wave absorption performance.

**3.2.1 Smith chart.** The impedance matching characteristic illustrates how much of the incident microwaves the absorber material can absorb. The Smith chart is another way to display impedance matching, with the center point indicating the matching point. The farther from the center of the circle, the

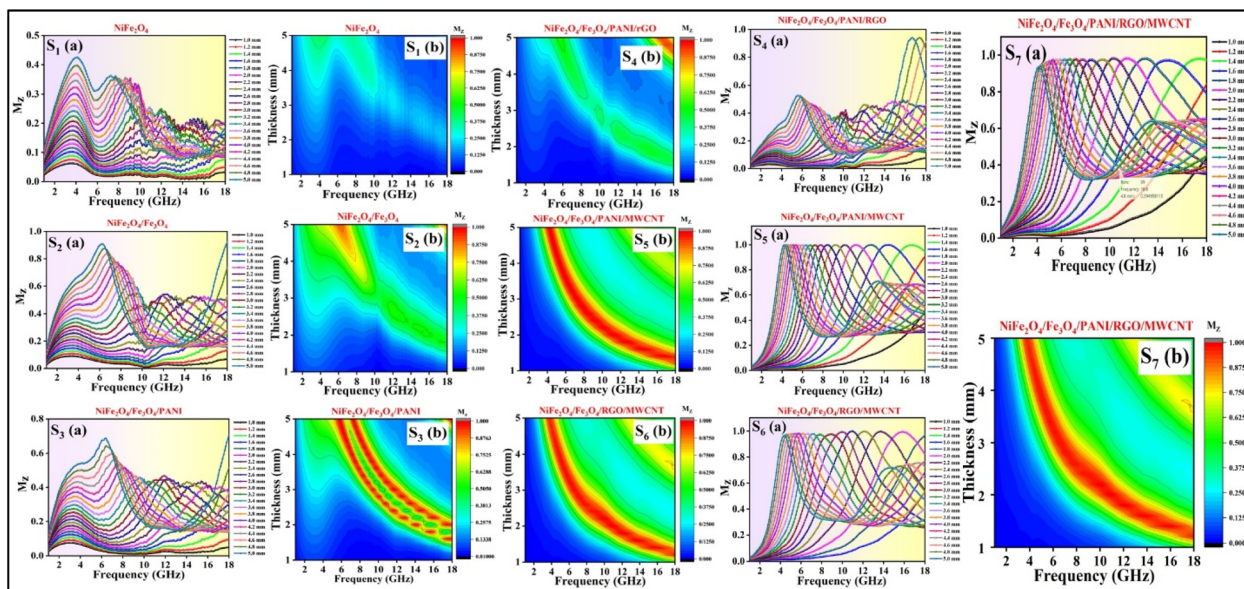


Fig. 14 2D, contour diagrams of input impedance matching coefficient for  $S_1$  (a, b),  $S_2$  (a, b),  $S_3$  (a, b),  $S_4$  (a, b),  $S_5$  (a, b),  $S_6$  (a, b),  $S_7$  (a, b).

poorer the impedance matching, and the more reflection occurs; conversely, the nearer to the center, the stronger the impedance matching. According to Fig. 15, the  $S_5$  sample exhibits the best impedance matching in the Ku band, which is consistent with the findings in Fig. 13 and 14. Additionally,  $S_6$  and  $S_7$  show relatively better impedance matching compared to the other samples. In Fig. 15, inductive features are detected in the upper semicircle of the Smith chart, while capacitance characteristics are displayed in the lower semicircle.<sup>61</sup> Moreover, by observing the path of the curve on the Smith chart, it can be noted that when the area enclosed by the curve is large, the impedance matching is better.<sup>61,62</sup>

**3.2.2 Absorber matching thickness.** Absorbing material thickness, in addition to parameters such as magnetic and dielectric loss, is a key factor that influences the performance of microwave absorption. According to the  $\lambda/4$  model, an increment in absorbent thickness should lead to a shift of the frequency (corresponding to  $RL_{\min}$ ) towards lower frequencies. This relationship is elucidated in eqn (6):<sup>63</sup>

$$t_m = \frac{n\lambda}{4} = \frac{nc}{4f_m \sqrt{|\mu_r||\epsilon_r|}} \quad (6)$$

where  $t_m$  represents the matching thickness,  $n$  is an odd number,  $f_m$  denotes the peak frequency,  $c$  is the speed of light,

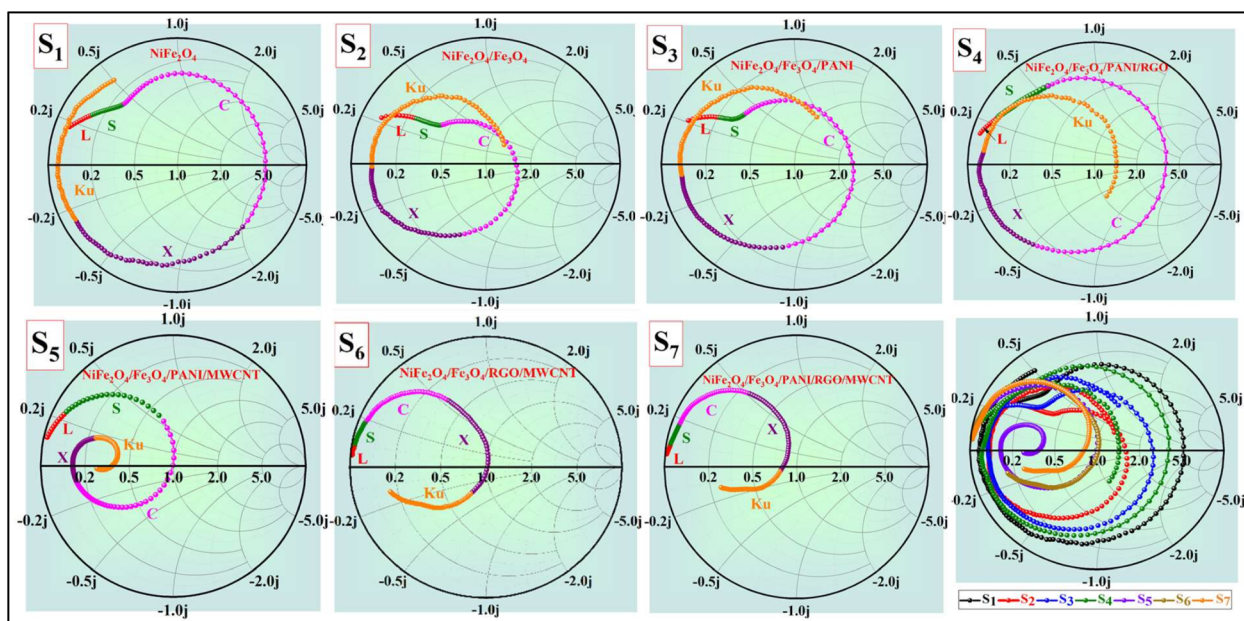


Fig. 15 The Smith chart characteristics of  $S_1$ ,  $S_2$ ,  $S_3$ ,  $S_4$ ,  $S_5$ ,  $S_6$ , and  $S_7$  are depicted with different colors to distinguish each frequency band. The frequency bands L, S, C, X, and Ku are represented by red, green, pink, purple, and orange colors respectively for clarity.

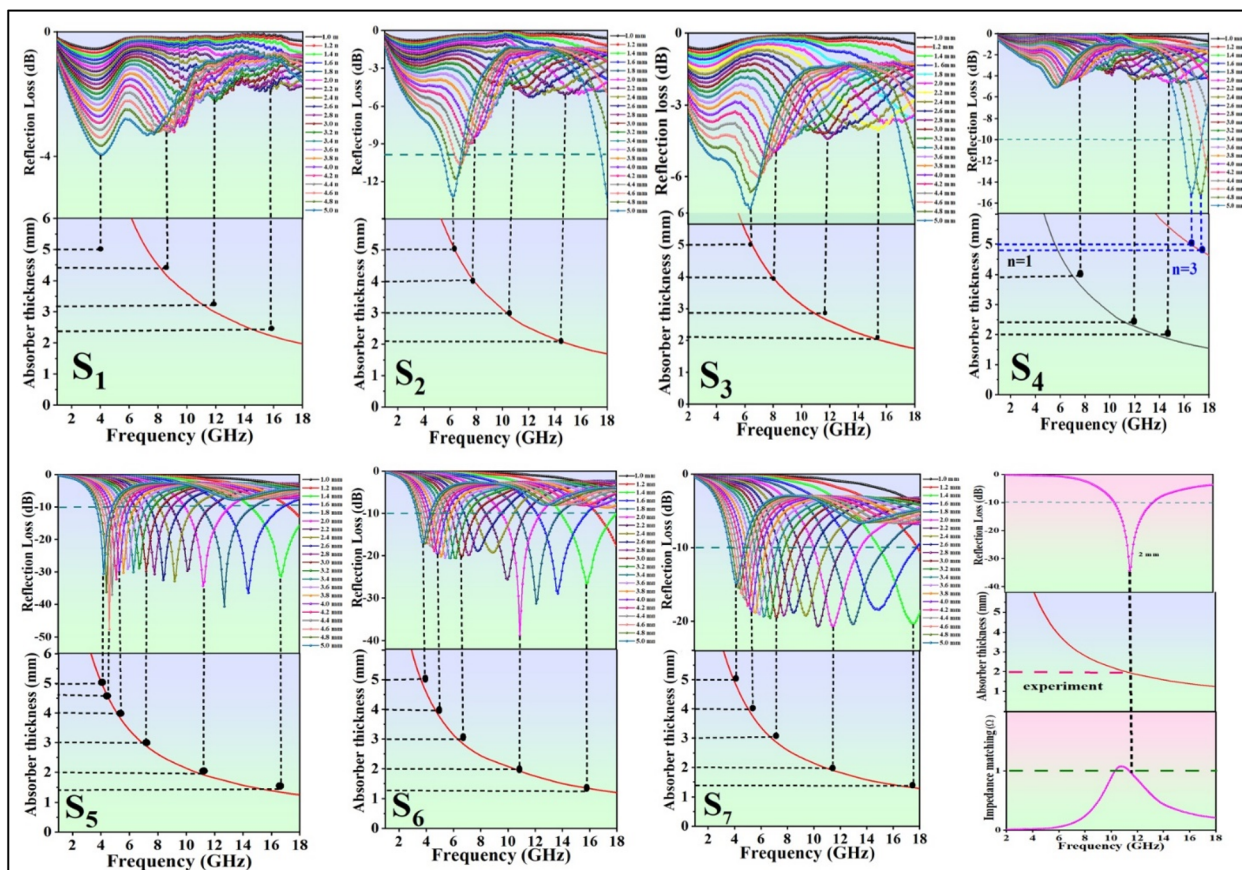


Fig. 16 RL curves and absorber thickness (experimental and fitted matching thicknesses) versus frequency of (S<sub>1</sub>) NiFe<sub>2</sub>O<sub>4</sub>, (S<sub>2</sub>) NiFe<sub>2</sub>O<sub>4</sub>/Fe<sub>3</sub>O<sub>4</sub>, (S<sub>3</sub>) NiFe<sub>2</sub>O<sub>4</sub>/Fe<sub>3</sub>O<sub>4</sub>/PANI, (S<sub>4</sub>) NiFe<sub>2</sub>O<sub>4</sub>/Fe<sub>3</sub>O<sub>4</sub>/PANI/RGO, (S<sub>5</sub>) NiFe<sub>2</sub>O<sub>4</sub>/Fe<sub>3</sub>O<sub>4</sub>/PANI/MWCNT, (S<sub>6</sub>) NiFe<sub>2</sub>O<sub>4</sub>/Fe<sub>3</sub>O<sub>4</sub>/RGO/MWCNT, (S<sub>7</sub>) NiFe<sub>2</sub>O<sub>4</sub>/Fe<sub>3</sub>O<sub>4</sub>/PANI/RGO/MWCNT.

and  $\lambda$  stands for the microwave wavelength. When the thickness of the absorber follows the conditions of the  $\lambda/4$  model as per eqn (6), a standing wave is generated, causing two anti-phase microwaves to cancel out at the interface between air and the absorbing material, resulting in an  $RL_{\min}$  peak. The RL curves of S<sub>1</sub>, S<sub>2</sub>, S<sub>3</sub>, S<sub>4</sub>, S<sub>5</sub>, S<sub>6</sub>, and S<sub>7</sub> with varying absorber thicknesses are depicted in Fig. 16, confirming the notable MA performance of the S<sub>5</sub> and S<sub>6</sub> samples.<sup>63</sup> Notably, the S<sub>4</sub> nanocomposite exhibits two peaks corresponding to  $n = 1$  and  $n = 3$  in the  $\lambda/4$  model.

To assess the impact of eddy current loss, the coefficient  $C_0$  is evaluated using eqn (7):

$$C_0 = \mu''(\mu')^{-2}f^{-1} \quad (7)$$

If eddy current loss is the sole mechanism contributing to magnetic loss within a specific frequency range, the coefficient  $C_0$  will remain constant. In Fig. 17a, it can be observed that between 2–10 GHz,  $C_0$  exhibits a diminishing trend, with fluctuations indicating the presence of natural resonance. However, beyond 10 GHz  $C_0$  remains constant, signifying the dominance of eddy current loss. Hence, eddy current losses are the primary cause of magnetic losses in the 10–18 GHz range, albeit at a relatively low magnitude.<sup>64</sup> At higher frequencies where fluctuations are not prominent, the impact of exchange resonance

on losses is minimal. Generally, ferrites with high electrical resistance exhibit low dielectric loss, resulting in low eddy current losses in nanocomposites containing ferrites.

The attenuation constant is another crucial parameter for assessing the absorption capabilities of absorbing materials, determined by the permittivity and permeability, as defined by eqn (8):

$$\alpha = \frac{\sqrt{2}\pi f}{c} \sqrt{(\epsilon''\mu'' - \mu'\epsilon') + \sqrt{(\epsilon''\mu'' - \mu'\epsilon')^2 + (\epsilon''\mu' + \mu''\epsilon')^2}} \quad (8)$$

The attenuation constants of the nanocomposites are illustrated in Fig. 17b. Among the samples, those containing MWCNT exhibit higher attenuation constants compared to the others. This indicates that the introduction of MWCNT into the nanocomposites has significantly enhanced their dielectric loss capabilities and attenuation constant ( $\alpha$ ), attributed to the notable increase in the electrical conductivity of the nanocomposites. While sample S<sub>6</sub> boasts the highest attenuation constant, its impedance matching value is 0.9, resulting in a weaker  $RL_{\min}$  compared to sample S<sub>5</sub>, which possesses an impedance matching value closer to 1 and consequently achieves the best RL performance. An ideal EM absorber should

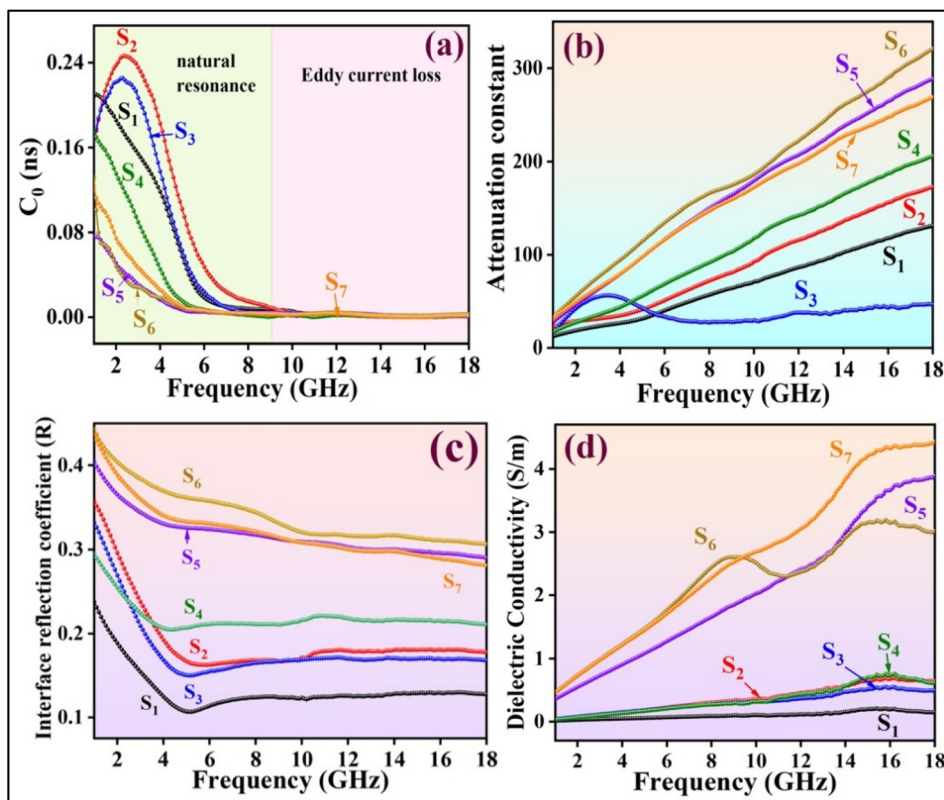


Fig. 17 (a): Eddy current loss coefficient, and (b): attenuation constant, (c): interface reflection coefficient, (d): dielectric conductivity of (S<sub>1</sub>) NiFe<sub>2</sub>O<sub>4</sub>, (S<sub>2</sub>) NiFe<sub>2</sub>O<sub>4</sub>/Fe<sub>3</sub>O<sub>4</sub>, (S<sub>3</sub>) NiFe<sub>2</sub>O<sub>4</sub>/Fe<sub>3</sub>O<sub>4</sub>/PANI, (S<sub>4</sub>) NiFe<sub>2</sub>O<sub>4</sub>/Fe<sub>3</sub>O<sub>4</sub>/PANI/RGO, (S<sub>5</sub>) NiFe<sub>2</sub>O<sub>4</sub>/Fe<sub>3</sub>O<sub>4</sub>/PANI/MWCNT, (S<sub>6</sub>) NiFe<sub>2</sub>O<sub>4</sub>/Fe<sub>3</sub>O<sub>4</sub>/RGO/MWCNT, (S<sub>7</sub>) NiFe<sub>2</sub>O<sub>4</sub>/Fe<sub>3</sub>O<sub>4</sub>/PANI/RGO/MWCNT.

have a high attenuation coefficient and near-perfect impedance matching (close to 1) simultaneously.<sup>50</sup>

EM waves typically reflect at the interface between the absorbing material and air. The interface reflection coefficient (*R*) represents the ratio of the reflected wave to the incident wave and is derived from eqn (9):<sup>65</sup>

$$R = \left( \frac{\sqrt{\frac{\mu_r}{\epsilon_r}} - 1}{\sqrt{\frac{\mu_r}{\epsilon_r}} + 1} \right)^2 \quad (9)$$

In Fig. 17c, it is evident that S<sub>6</sub> exhibits the highest surface reflection coefficient, indicating the effective dissipation of EM waves. S<sub>7</sub>, S<sub>6</sub>, and S<sub>5</sub> display higher *R* coefficients compared to the other samples, highlighting their superior ability to absorb and attenuate electromagnetic waves.<sup>65</sup>

In Fig. 17d, it is observed that the dielectric conductive loss is directly proportional to the conductivity of the absorbents. The incorporation of conductive components in the nanocomposite formulation can enhance the conductive loss, as calculated using eqn (10):<sup>51</sup>

$$\sigma = \omega \epsilon_0 \epsilon'' \quad (10)$$

The presence of the conductive material RGO has increased the dielectric conductivity of nano composition S<sub>4</sub> compared to

S<sub>1</sub>, S<sub>2</sub>, and S<sub>3</sub>. However, MWCNT plays a significant role in improving conductive loss, leading to higher conductive loss in S<sub>5</sub>, S<sub>6</sub>, and S<sub>7</sub>.

Fig. 18 presents 3D and 2D Cole–Cole curves for all samples. Specifically, Fig. 18(h) and (i) display 2D Cole–Cole curves for S<sub>1</sub>, S<sub>2</sub>, S<sub>3</sub>, S<sub>4</sub>, S<sub>5</sub>, S<sub>6</sub>, and S<sub>7</sub>. The polarization-relaxation phenomena are fundamental dielectric loss mechanisms that absorb electromagnetic microwaves, as described by the Cole–Cole model.<sup>66,67</sup> In the Cole–Cole curve, each semicircle represents a Debye relaxation process. Fig. 18 illustrates that all samples exhibit multiple semicircles, indicating multiple relaxations. These multiple relaxations include interface polarization and dipolar polarization.<sup>42</sup> Another dielectric loss mechanism is identified by the deviation from the circular state, attributed to conduction loss.<sup>4</sup> This conduction loss originates from the migration of electrons within the conductive network of RGO and MWCNT, with PANI playing a minor role, ultimately enhancing conduction loss.

The Cole–Cole relation is mathematically represented by eqn (11):

$$\left( \epsilon' - \frac{\epsilon_s + \epsilon_\infty}{2} \right)^2 + (\epsilon'')^2 = \left( \frac{\epsilon_s - \epsilon_\infty}{2} \right)^2 \quad (11)$$

where  $\epsilon_s$  is the static permittivity, and  $\epsilon_\infty$  is the relative permittivity in the high-frequency limit.<sup>44</sup> In Fig. 18(h), deviated semicircles with linear tails illustrate the multiple polarization

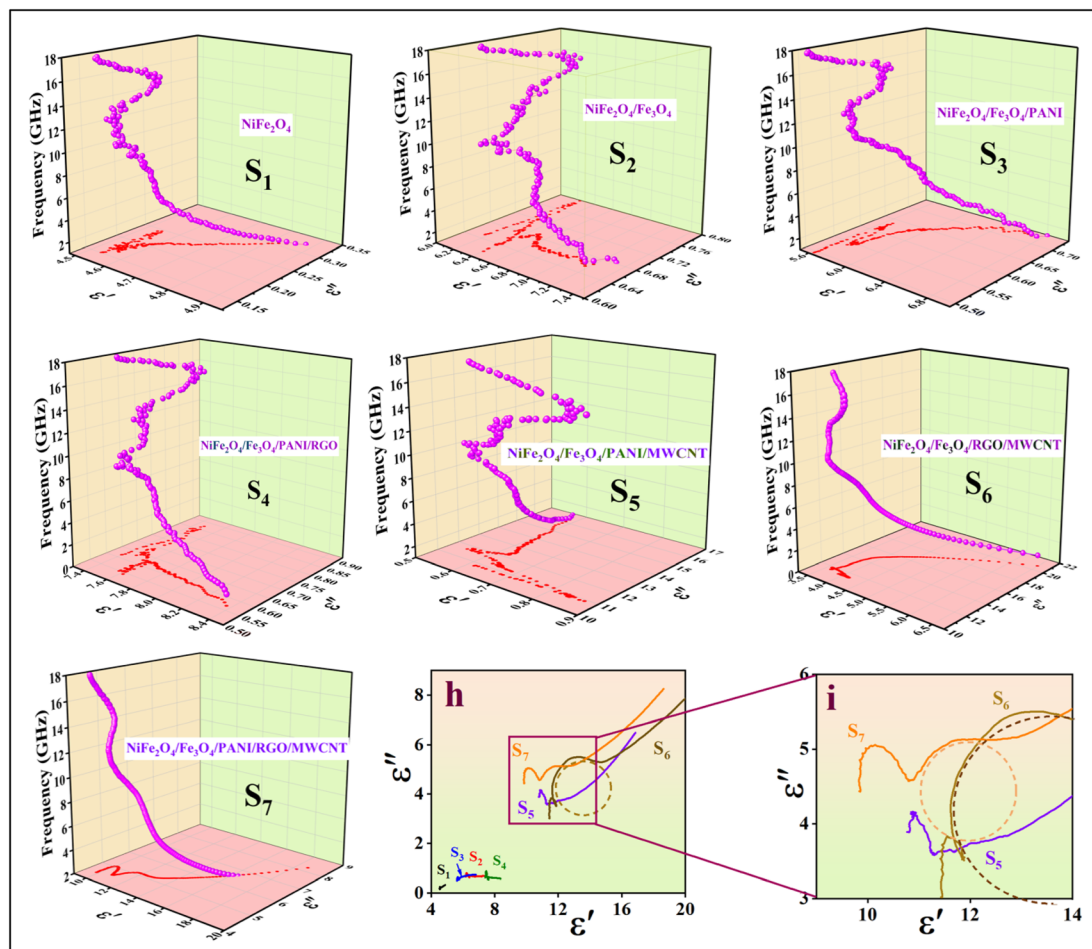


Fig. 18 3D Cole–Cole curves for (S<sub>1</sub>) NiFe<sub>2</sub>O<sub>4</sub>, (S<sub>2</sub>) NiFe<sub>2</sub>O<sub>4</sub>/Fe<sub>3</sub>O<sub>4</sub>, (S<sub>3</sub>) NiFe<sub>2</sub>O<sub>4</sub>/Fe<sub>3</sub>O<sub>4</sub>/PANI, (S<sub>4</sub>) NiFe<sub>2</sub>O<sub>4</sub>/Fe<sub>3</sub>O<sub>4</sub>/PANI/RGO, (S<sub>5</sub>) NiFe<sub>2</sub>O<sub>4</sub>/Fe<sub>3</sub>O<sub>4</sub>/PANI/MWCNT, (S<sub>6</sub>) NiFe<sub>2</sub>O<sub>4</sub>/Fe<sub>3</sub>O<sub>4</sub>/RGO/MWCNT, (S<sub>7</sub>) NiFe<sub>2</sub>O<sub>4</sub>/Fe<sub>3</sub>O<sub>4</sub>/PANI/RGO/MWCNT, (h) 2D curves of all samples, (i) 2D curves of the samples contains MWCNT.

and conduction losses in the nanocomposite samples. The S<sub>4</sub> sample shows a small tail, indicating the role of the conductive RGO sheets. Conversely, the samples containing MWCNT (S<sub>5</sub>, S<sub>6</sub>, S<sub>7</sub>) exhibit long tails, highlighting the significant contribution of conduction loss in dissipating EM waves. The Cole–Cole diagram of S<sub>1</sub> displays a semicircle without a linear tail, indicating that polarization-relaxation predominantly drives the polarization loss mechanisms. Therefore, dielectric-conductive loss emerges as a key factor in microwave absorption in this study. To delve deeper into the polarization-relaxation loss, the relationship between the real part and the imaginary part of permittivity can be explored using eqn (12):

$$\varepsilon' = \frac{1}{2\pi\tau} \frac{\varepsilon''}{f} + \varepsilon_{\infty} \quad (12)$$

In cases where dielectric loss is governed by the polarization-relaxation mechanism, the relaxation time ( $\tau$ ) can be determined by the slope of the linear function of  $\varepsilon'$  versus  $\varepsilon''/f$  using eqn (12), as illustrated in Fig. 19. The varying slope of the curve is attributed to the flexible orientation of the dipoles. We identified and analyzed three fitted lines for each curve using

linear regression to derive  $\tau$ . Diverse relaxation times signify distinct polarization-relaxation phenomena contributing to dielectric loss and attenuating microwaves.<sup>51</sup>

**3.2.3 Radar cross-section (RCS).** In the actual application, the microwave attenuation capabilities of all the samples were evaluated based on the RCS values of PEC coated with the products. These values were calculated using CST simulation software. The PEC substrate was initially defined and placed within a  $50 \times 50 \times 2.0$  mm<sup>3</sup> environment.<sup>68</sup> Following the simulation, the 3D simulated color maps and 2D RCS values ranging from 0° to 180° are displayed in Fig. 20. The electromagnetic wave is directed toward the PEC coated with samples, resulting in RCS values that are lower than those of the pristine PEC. Scattering of the incident wave from the PEC is greatly reduced following the application of the MAMs. The reduction in RCS values (the RCS values of the PEC minus those of the PEC coated with the samples) of the PEC coated with the samples is observed as 2.26 dB m<sup>2</sup>, 3.0 dB m<sup>2</sup>, and 4.68 dB m<sup>2</sup> for S<sub>6</sub>, S<sub>7</sub> and S<sub>5</sub>, respectively, at  $\theta = 90^\circ$  for frequency 10.9 GHz,  $\phi = 90^\circ$  and direction XOZ. The simulation results demonstrate that the sample exhibits enhanced EM wave dissipation capabilities,

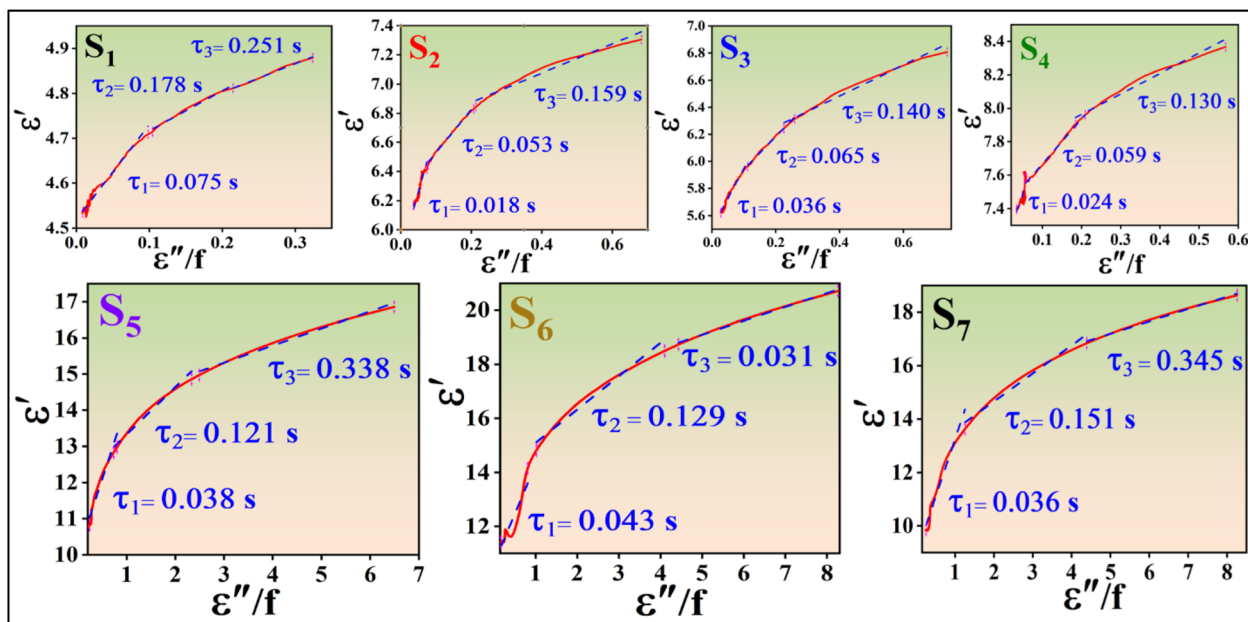


Fig. 19  $\epsilon'$  versus  $\epsilon''/f$  (solid red line) and relaxation times obtained from the slopes of the fitted lines (dashed blue line) of (S<sub>1</sub>) NiFe<sub>2</sub>O<sub>4</sub>, (S<sub>2</sub>) NiFe<sub>2</sub>O<sub>4</sub>/Fe<sub>3</sub>O<sub>4</sub>, (S<sub>3</sub>) NiFe<sub>2</sub>O<sub>4</sub>/Fe<sub>3</sub>O<sub>4</sub>/PANI, (S<sub>4</sub>) NiFe<sub>2</sub>O<sub>4</sub>/Fe<sub>3</sub>O<sub>4</sub>/PANI/RGO, (S<sub>5</sub>) NiFe<sub>2</sub>O<sub>4</sub>/Fe<sub>3</sub>O<sub>4</sub>/PANI/MWCNT, (S<sub>6</sub>) NiFe<sub>2</sub>O<sub>4</sub>/Fe<sub>3</sub>O<sub>4</sub>/RGO/MWCNT, (S<sub>7</sub>) NiFe<sub>2</sub>O<sub>4</sub>/Fe<sub>3</sub>O<sub>4</sub>/PANI/RGO/MWCNT.

effectively reducing microwave scattering. As a result, our fabricated samples show promise as potential candidates for real-world applications in the field of EM waves.

**3.2.4 MA mechanisms.** Our nanocomposites are formed by components with varying conductivity and permittivity, leading to the accumulation of charges at heterojunction interfaces such as between RGO and MWCNT, NiFe<sub>2</sub>O<sub>4</sub> and Fe<sub>3</sub>O<sub>4</sub>, RGO and NiFe<sub>2</sub>O<sub>4</sub>/Fe<sub>3</sub>O<sub>4</sub>, and MWCNT, NiFe<sub>2</sub>O<sub>4</sub>/Fe<sub>3</sub>O<sub>4</sub>, and RGO. The presence of defects and functional groups in RGO sheets induces dipole polarization. Conductive loss may occur due to

electron migration within the conductive sheets of RGO and MWCNT, as well as electron hopping between RGO and MWCNT, MWCNTs, and different RGO sheets. The combination of the three conductive materials (MWCNT, PANI, RGO) forms a conductive network that enhances the propagation of EM waves. The layered structure of PANI further boosts EM wave propagation. The composition of multiple nanocomposites leads to internal reflections. The magnetic property of Fe<sub>3</sub>O<sub>4</sub> results in the generation of eddy currents when the prepared nanocomposites are subjected to a periodic magnetic field of

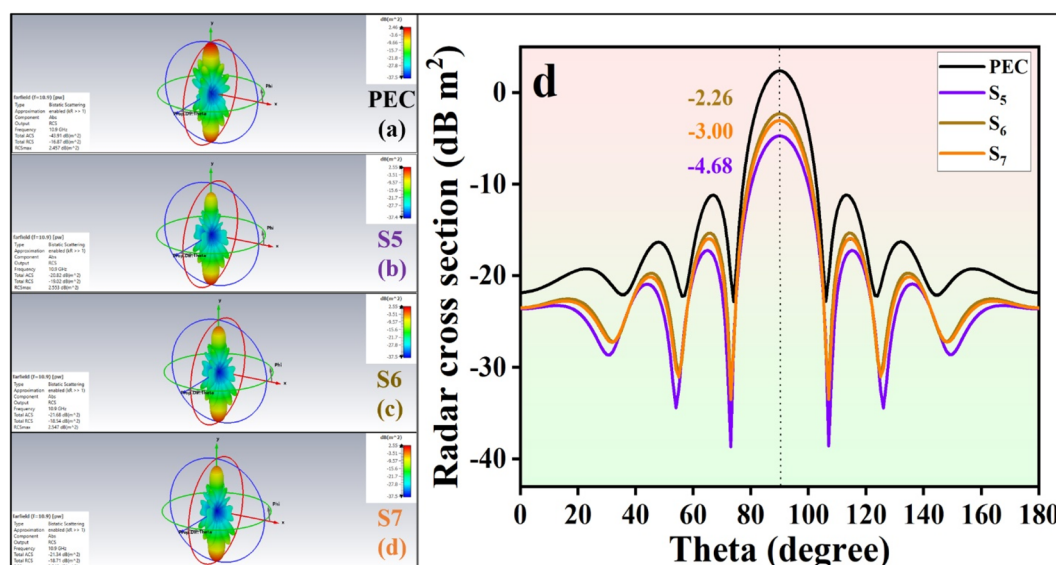


Fig. 20 3D intensity images of the reflected signal PEC (a), PEC coated with S<sub>5</sub>, S<sub>6</sub>, S<sub>7</sub>, and RCS simulated curves of the samples at different scanning angles (d).

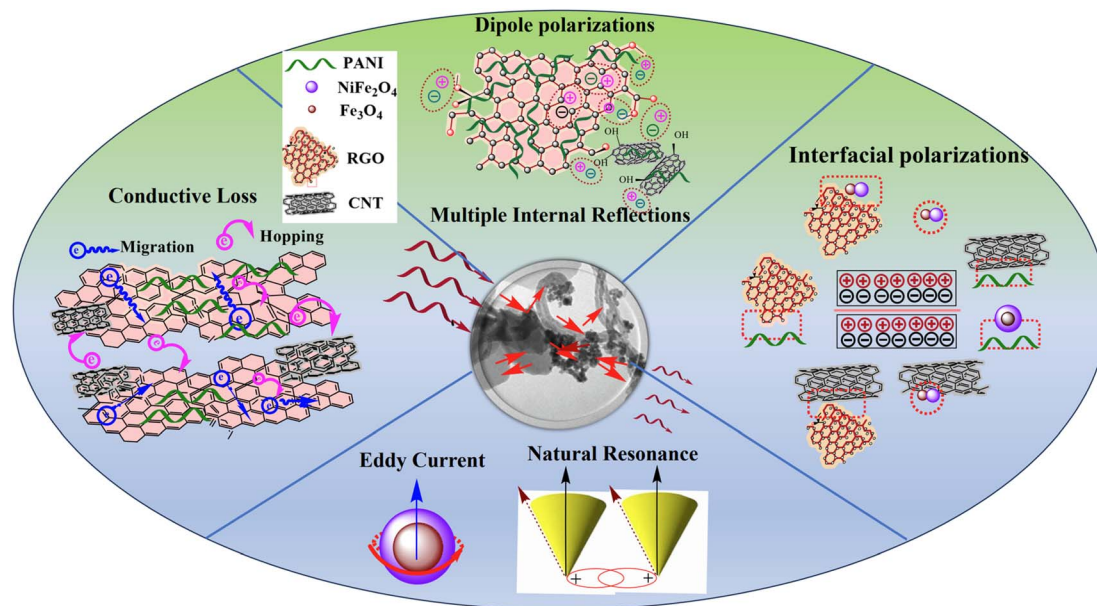


Fig. 21 Schematic diagram of MA mechanisms of interfacial polarization, dipole polarization, conduction loss, and magnetic loss for  $\text{NiFe}_2\text{O}_4/\text{Fe}_3\text{O}_4/\text{PANI}/\text{RGO}/\text{MWCNT}$ .

EM waves. Fig. 21 depicts the schematic diagram showcasing different loss mechanisms such as interfacial polarization, dipole polarization, conduction loss, and magnetic loss for  $\text{NiFe}_2\text{O}_4/\text{Fe}_3\text{O}_4/\text{PANI}/\text{RGO}/\text{MWCNT}$ .

## 4 Conclusion

In summary, the nanocomposites  $\text{NiFe}_2\text{O}_4$  ( $S_1$ ),  $\text{NiFe}_2\text{O}_4/\text{Fe}_3\text{O}_4$  ( $S_2$ ),  $\text{NiFe}_2\text{O}_4/\text{Fe}_3\text{O}_4/\text{PANI}$  ( $S_3$ ),  $\text{NiFe}_2\text{O}_4/\text{Fe}_3\text{O}_4/\text{PANI}/\text{RGO}$  ( $S_4$ ),  $\text{NiFe}_2\text{O}_4/\text{Fe}_3\text{O}_4/\text{PANI}/\text{MWCNT}$  ( $S_5$ ),  $\text{NiFe}_2\text{O}_4/\text{Fe}_3\text{O}_4/\text{RGO}/\text{MWCNT}$  ( $S_6$ ), and  $\text{NiFe}_2\text{O}_4/\text{Fe}_3\text{O}_4/\text{PANI}/\text{RGO}/\text{MWCNT}$  ( $S_7$ ) were successfully synthesized using hydrothermal, coprecipitation, and *in situ* polymerization methods. The addition of MWCNT to the samples significantly enhanced their microwave absorption performance. Notably, sample  $S_5$  exhibited outstanding reflection loss of  $-47.5$  dB at 4.6 GHz with a matching thickness of 4.6 mm and the best effective absorption bandwidth of 4 GHz for  $d = 1.6$  mm. The  $\text{RL}_{\min}$  of sample  $S_5$  remained below  $-10$  dB for various thicknesses and frequencies, indicating its excellent absorption of electromagnetic waves across the C, X, and Ku bands. Sample  $S_6$  demonstrated favorable microwave absorption properties with an EAB of 4 GHz at  $d = 1.4$  mm and an  $\text{RL}_{\min} = -38.7$  dB at 10.9 GHz for a thickness of 2 mm. The widest EAB of 4.8 GHz was achieved by sample  $S_7$  at  $d = 1.6$  mm, covering more than one-fourth of the frequency band independently. Similarly, the CST simulation results confirm that the three synthesized products ( $S_5$ ,  $S_6$ , and  $S_7$ ) are capable of dissipating microwave energy and have the potential for real-world practical applications. The synergistic effects of RGO, MWCNT, and PANI in creating an extended conductive network are believed to be responsible for this phenomenon. The heterogeneous structure of the prepared nanocomposites acts as a broadband absorber, absorbing over 99% of incident

electromagnetic waves. The careful selection of ingredients and the preparation method resulted in a well-designed material rich in interfaces, void spaces, and interconnected conductive networks, leading to the dissipation of microwaves through a combination of dielectric, conductive, and magnetic losses.

## Abbreviations

EAB	effective absorption bandwidth
EDS	energy-dispersive X-ray spectroscopy
EM	electromagnetic
FESEM	field emission scanning electron microscopy
FTIR	Fourier transform infrared
GO	graphene oxide
MA	microwave absorption
MAMs	microwave-absorbing materials
MWCNT	multi-walled carbon nanotube
PANI	polyaniline
PEC	perfect electric conductor
RCS	radar cross-section
RGO	reduced graphene oxide
RL	reflection loss
RT	room temperature
TEM	transmission electron microscopy
VSM	vibrating-sample magnetometry
XRD	X-ray diffraction

## Symbols

$c$	speed of the electromagnetic wave
$f$	frequency of the microwave
$\lambda$	wavelength of the microwave

$\tan \delta_\epsilon$	dielectric loss tangent
$\tan \delta_\mu$	magnetic loss tangent
$t_m$	matching thickness
$Z_0$	impedance of free space
$Z_{in}$	input impedance
$\alpha$	attenuation coefficient
$\epsilon_0$	permittivity of free space
$\epsilon_r$	relative permittivity
$\epsilon'$	real part of relative permittivity
$\epsilon''$	imaginary part of relative permittivity
$\mu_0$	permeability of free space
$\mu_r$	relative permeability
$\mu'$	real part of relative permeability
$\mu''$	imaginary part of relative permeability
$\sigma$	electrical conductivity

## Data availability

All data generated or analyzed during this study are included in this article.

## Conflicts of interest

The authors declare no competing interests.

## Acknowledgements

The authors thank Prof. J. Teixeira for his assistance with the manuscript and valuable comments.

## References

- 1 F. Ebrahimi-Tazangi, M. Maazallahi, P. Livreri and J. Seyed-Yazdi, MnFe<sub>2</sub>O<sub>4</sub>/Fe<sub>3</sub>O<sub>4</sub>/PANI/rGO heterogeneous nanocomposites: Outstanding dual-broadband nano-coating microwave absorbers, *J. Alloys Compd.*, 2024, **1002**, 175149, DOI: [10.1016/j.jallcom.2024.175149](#).
- 2 L. Liang, X. Yang, Ch. Li, R. Yu, B. Zhang, Y. Yang and G. Ji, MXene-Enabled Pneumatic Multiscale Shape Morphing for Adaptive, Programmable and Multimodal Radar-infrared Compatible Camouflage, *Adv. Mater.*, 2024, **36**, 2313939, DOI: [10.1002/adma.202313939](#).
- 3 R. Liu, M. Miao, Y. Li, J. Zhang, S. Cao and X. Feng, Ultrathin Biomimetic Polymeric Ti<sub>3</sub>C<sub>2</sub>T<sub>x</sub> MXene Composite Films for Electromagnetic Interference Shielding, *ACS Appl. Mater. Interfaces*, 2018, **10**, 44787–44795, DOI: [10.1021/acsami.8b18347](#).
- 4 B. Zhan, Y. Qu, X. Qi, J. Ding, J. Shao, X. Gong, J. Yang, Y. Chen, Q. Peng, W. Zhong and H. Lv, Mixed-Dimensional Assembly Strategy to Construct Reduced Graphene Oxide/Carbon Foams Heterostructures for Microwave Absorption, Anti-Corrosion and Thermal Insulation, *Nano-Micro Lett.*, 2024, **16**, 221, DOI: [10.1007/s40820-024-01447-9](#).
- 5 S. Golchinvafo, S. M. Masoudpanah and S. Alamolhoda, Ultra-broadband FeNi<sub>3</sub>/NiZnFe<sub>2</sub>O<sub>4</sub>/ZnO composite powders for microwave absorption, *J. Mater. Res. Technol.*, 2022, **21**, 1737–1748, DOI: [10.1016/j.jmrt.2022.09.123](#).
- 6 Y. Cao, N. Forouk, N. Mortezaei, A. V. Yumasher and M. N. Akhtar, Arabmarkadeh, Investigation on microwave absorption characteristics of ternary MWCNTs/CoFe<sub>2</sub>O<sub>4</sub>/FeCo nanocomposite coated with conductive PEDOT-Polyaniline Co-polymers, *Ceram. Int.*, 2021, **47**(9), 12244–12251, DOI: [10.1016/j.ceramint.2021.01.073](#).
- 7 J. Xue, H. Zhang, J. Zhao, X. Ou and Y. Ling, Characterization and microwave absorption of spinel MFe<sub>2</sub>O<sub>4</sub> (M= Mg, Mn, Zn) nanoparticles prepared by a facile oxidation-precipitation process, *J. Magn. Magn. Mater.*, 2020, **514**, 167168, DOI: [10.1016/j.jmmm.2020.167168](#).
- 8 D. Mandal and M. Mandal, Electromagnetic wave attenuation properties of MFe<sub>2</sub>O<sub>4</sub> (M= Mn, Fe, Co, Ni, Cu, Zn) nano-hollow spheres in search of an efficient microwave absorber, *J. Magn. Magn. Mater.*, 2021, **536**, 168127, DOI: [10.1016/j.jmmm.2021.168127](#).
- 9 A. Toghan, M. Khairy, E. M. Kamar and M. A. Mousa, Effect of particle size and morphological structure on the physical properties of NiFe<sub>2</sub>O<sub>4</sub> for supercapacitor application, *J. Mater. Res. Technol.*, 2022, **19**, 3521–3535, DOI: [10.1016/j.jmrt.2022.06.095](#).
- 10 S. Li, J. Luo, J. Wang, Y. Zhu, J. Feng, N. Fu, H. Wang, Y. Guo, D. Tian, Y. Zheng, S. Sun, C. Zhang, K. Chen, S. Mu and Y. Huang, Hybrid supercapacitors using metal-organic framework derived nickel-sulfur compounds, *J. Colloid Interface Sci.*, 2024, **669**, 265–274, DOI: [10.1016/j.jcis.2024.04.205](#).
- 11 P. Balasubramanian, S. B. He, A. Jansirani, H. H. Deng, H. P. Peng, X. H. Xia, *et al.*, Engineering of oxygen vacancies regulated core-shell N-doped carbon@ NiFe<sub>2</sub>O<sub>4</sub> nanospheres: A superior bifunctional electrocatalyst for boosting the kinetics of oxygen and hydrogen evolution reactions, *Chem. Eng. J.*, 2021, **405**, 126732, DOI: [10.1016/j.cej.2020.126732](#).
- 12 Y. Zhang, X. Wang and M. Cao, Confinedly implanted NiFe<sub>2</sub>O<sub>4</sub>-RGO: Cluster tailoring and highly tunable electromagnetic properties for selective-frequency microwave absorption, *Nano Res.*, 2018, **11**(3), 1426–1436, DOI: [10.1007/s12274-017-1758-1](#).
- 13 M. Yuan, M. Zhou and H. Fu, Synergistic microstructure of sandwich-like NiFe@ SiO<sub>2</sub>@ MXene nanocomposites for enhancement of microwave absorption in the whole Ku-band, *Composites, Part B*, 2021, **224**, 109178, DOI: [10.1016/j.compositesb.2021.109178](#).
- 14 A. Kumar, A. K. Singh, M. Tomar, V. Gupta, P. Kumar and K. Singh, Electromagnetic interference shielding performance of lightweight NiFe<sub>2</sub>O<sub>4</sub>/RGO nanocomposite in X-band frequency range, *Ceram. Int.*, 2020, **46**(10), 15473–15481, DOI: [10.1016/j.ceramint.2020.03.092](#).
- 15 Q. A. Alsulami, Structural, dielectric, and magnetic studies based on MWCNTs/NiFe<sub>2</sub>O<sub>4</sub>/ZnO nanoparticles dispersed in polymer PVA/PEO for electromagnetic applications, *J. Mater. Sci.: Mater. Electron.*, 2021, **32**(3), 2906–2924, DOI: [10.1007/s10854-020-05043-6](#).
- 16 F. Ebrahimi-Tazangi, S. H. Hekmatara and J. Seyed-Yazdi, Synthesis and remarkable microwave absorption properties of amine-functionalized magnetite/graphene oxide

- nanocomposites, *J. Alloys Compd.*, 2019, **809**, 151779, DOI: [10.1016/j.jallcom.2019.151779](https://doi.org/10.1016/j.jallcom.2019.151779).
- 17 H. Cai, C. Feng, H. Xiao and B. Cheng, Synthesis of Fe<sub>3</sub>O<sub>4</sub>/RGO@ PANI with three-dimensional flower-like nanostructure and microwave absorption properties, *J. Alloys Compd.*, 2022, **893**, 162227, DOI: [10.1016/j.jallcom.2021.162227](https://doi.org/10.1016/j.jallcom.2021.162227).
  - 18 Y. Wang, L. Yao, Q. Zheng and M. S. Cao, Graphene-wrapped multilocalized nickel ferrite: A highly efficient electromagnetic attenuation material for microwave absorbing and green shielding, *Nano Res.*, 2022, 1–10, DOI: [10.1007/s12274-022-4428-x](https://doi.org/10.1007/s12274-022-4428-x).
  - 19 P. Heidari and S. Masoudpanah, A facial synthesis of MgFe<sub>2</sub>O<sub>4</sub>/RGO nanocomposite powders as a high-performance microwave absorber, *J. Alloys Compd.*, 2020, **834**, 155166, DOI: [10.1016/j.jallcom.2020.155166](https://doi.org/10.1016/j.jallcom.2020.155166).
  - 20 Q. Huang, Y. Zhao, Y. Wu, M. Zhou, S. Tan, S. Tang, *et al.*, A dual-band transceiver with excellent heat insulation property for microwave absorption and low infrared emissivity compatibility, *Chem. Eng. J.*, 2022, 137279, DOI: [10.1016/j.cej.2022.137279](https://doi.org/10.1016/j.cej.2022.137279).
  - 21 F. Yang, Y. Huang, X. Han, S. Zhang, M. Yu, J. Zhang, *et al.*, Covalent Bonding of MXene/Reduced Graphene Oxide Composites for Efficient Electromagnetic Wave Absorption, *ACS Appl. Nano Mater.*, 2023, **6**(5), 3367–3377, DOI: [10.1021/acsanm.2c05150](https://doi.org/10.1021/acsanm.2c05150).
  - 22 G. Salimbeygi, K. Nasouri, A. Mousavi Shashtari, R. Malek and F. Mazaheri, Microwave absorption properties of polyaniline/poly (vinyl alcohol)/multi-walled carbon nanotube composites in thin film and nanofiber layer structures, *Macromol. Res.*, 2015, **23**(8), 741–748, DOI: [10.1007/s13233-015-3102-5](https://doi.org/10.1007/s13233-015-3102-5).
  - 23 J. Xu, C. Bian, J. Sun, D. Liu, X. Wang, Z. Xue, *et al.*, Heterostructure tailoring of carbon nanotubes grown on prismatic NiCo clusters for high-efficiency electromagnetic absorption, *J. Colloid Interface Sci.*, 2023, **634**, 185–194, DOI: [10.1016/j.jcis.2022.12.037](https://doi.org/10.1016/j.jcis.2022.12.037).
  - 24 B. G. Soares, G. M. Barra and T. Indrusiak, Conducting polymeric composites based on intrinsically conducting polymers as electromagnetic interference shielding/microwave absorbing materials—A review, *J. Compos. Sci.*, 2021, **5**(7), 173, DOI: [10.3390/JCS5070173](https://doi.org/10.3390/JCS5070173).
  - 25 S. S. Hassan, A. H. Kamel, A. A. Hassan, A. E. E. Amr, H. A. El-Naby, M. A. Al-Omar, *et al.*, CuFe<sub>2</sub>O<sub>4</sub>/polyaniline (PANI) nanocomposite for the hazard mercuric ion removal: synthesis, characterization, and adsorption properties study, *Molecules*, 2020, **25**(12), 2721, DOI: [10.3390/molecules25122721](https://doi.org/10.3390/molecules25122721).
  - 26 F. Ebrahimi-Tazangi, J. Seyed-Yazdi and S. H. Hekmatara,  $\alpha$ -Fe<sub>2</sub>O<sub>3</sub>@ CoFe<sub>2</sub>O<sub>4</sub>/GO nanocomposites for broadband microwave absorption by surface/interface effects, *J. Alloys Compd.*, 2022, **900**, 163340, DOI: [10.1016/j.jallcom.2021.163340](https://doi.org/10.1016/j.jallcom.2021.163340).
  - 27 M. Zhang, L. Chen, Y. Yu, X. Meng and J. Xiang, Carbon nanofiber supported cobalt ferrite composites with tunable microwave absorption properties, *Ceram. Int.*, 2021, **47**(7), 9392–9399, DOI: [10.1016/j.ceramint.2020.12.071](https://doi.org/10.1016/j.ceramint.2020.12.071).
  - 28 W. Ma, R. Yang, Z. Yang, C. Duan and T. Wang, Synthesis of reduced graphene oxide/zinc ferrite/nickel nanohybrids: As a lightweight and high-performance microwave absorber in the low frequency, *J. Mater. Sci.: Mater. Electron.*, 2019, **30**(20), 18496–18505, DOI: [10.1007/s10854-019-02203-1](https://doi.org/10.1007/s10854-019-02203-1).
  - 29 Q. Li, W. Guo, X. Kong, J. Xu, Ch. Xu, Y. Chen, J. Chen, X. Jia and Y. Ding, MnFe<sub>2</sub>O<sub>4</sub>/rGO/Diatomite composites with excellent wideband electromagnetic microwave absorption, *J. Alloys Compd.*, 2023, **941**, 168851, DOI: [10.1016/j.jallcom.2023.168851](https://doi.org/10.1016/j.jallcom.2023.168851).
  - 30 Y. Zhang, J. Liu, Y. Zhang, J. Liu and Y. Duan, Facile synthesis of hierarchical nanocomposites of aligned polyaniline nanorods on reduced graphene oxide nanosheets for microwave absorbing materials, *RSC Adv.*, 2017, **7**(85), 54031–54038, DOI: [10.1039/c7ra08794b](https://doi.org/10.1039/c7ra08794b).
  - 31 A. Henaish, B. I. Salem, T. M. Meaz, Y. A. Alibwaini, A. W. Ajlouni, O. M. Hemeda, *et al.*, Synthesize, characterization, dielectric, linear and nonlinear optical properties of Ni–Al Ferrite/PANI nanocomposite film, *Opt. Mater.*, 2021, **119**, 111397, DOI: [10.1016/j.optmat.2021.111397](https://doi.org/10.1016/j.optmat.2021.111397).
  - 32 L. Xie, Z. Ren, P. Zhu, J. Xu, D. Luo and J. Lin, A novel CeO<sub>2</sub>–TiO<sub>2</sub>/PANI/NiFe<sub>2</sub>O<sub>4</sub> magnetic photocatalyst: Preparation, characterization and photodegradation of tetracycline hydrochloride under visible light, *J. Solid State Chem.*, 2021, **300**, 122208, DOI: [10.1016/j.jssc.2021.122208](https://doi.org/10.1016/j.jssc.2021.122208).
  - 33 R. Shu, G. Zhang, J. Zhang, X. Wang, M. Wang, Y. Gan, *et al.*, Fabrication of reduced graphene oxide/multi-walled carbon nanotubes/zinc ferrite hybrid composites as high-performance microwave absorbers, *J. Alloys Compd.*, 2018, **736**, 1–11, DOI: [10.1016/j.jallcom.2017.11.084](https://doi.org/10.1016/j.jallcom.2017.11.084).
  - 34 M. Kooti, A. Naghdi Sadeh, Kh. Gheisari and A. Figuerola, Synthesis, characterization, and performance of nanocomposites containing reduced graphene oxide, polyaniline, and cobalt ferrite, *Phys. B*, 2021, **612**, 412974, DOI: [10.1016/j.physb.2021.412974](https://doi.org/10.1016/j.physb.2021.412974).
  - 35 Y. Wu, R. Shu, C. Li, C. Guo, G. Zhang, J. Zhang, *et al.*, Design and electromagnetic wave absorption properties of reduced graphene oxide/multi-walled carbon nanotubes/nickel ferrite ternary nanocomposites, *J. Alloys Compd.*, 2019, **784**, 887–896, DOI: [10.1016/j.jallcom.2019.01.139](https://doi.org/10.1016/j.jallcom.2019.01.139).
  - 36 J. A. Oyetade, R. Lazaro Machunda and A. Hilonga, Functional impacts of polyaniline in composite matrix of photocatalysts: an instrumental overview, *RSC Adv.*, 2023, **13**, 15467–15489, DOI: [10.1039/d3ra01243c](https://doi.org/10.1039/d3ra01243c).
  - 37 Q. Ban, Y. Li, Y. Qin, Y. Zheng, X. Xie, Z. Yu, *et al.*, Hierarchical engineering of Large-caliber carbon Nanotube/Mesoporous Carbon/Fe<sub>3</sub>C nanoparticle hybrid nanocomposite towards Ultra-lightweight electromagnetic microwave absorber, *J. Colloid Interface Sci.*, 2022, **616**, 618–630, DOI: [10.1016/j.jcis.2022.02.104](https://doi.org/10.1016/j.jcis.2022.02.104).
  - 38 Y. Ding, Q. Liao, S. Liu, H. Guo, Y. Sun, G. Zhang, *et al.*, Reduced graphene oxide functionalized with cobalt ferrite nanocomposites for enhanced efficient and lightweight electromagnetic wave absorption, *Sci. Rep.*, 2016, **6**(1), 1–9, DOI: [10.1038/srep32381](https://doi.org/10.1038/srep32381).

- 39 J. Yan, Y. Huang, X. Chen and C. Wei, Conducting polymers-NiFe<sub>2</sub>O<sub>4</sub> coated on reduced graphene oxide sheets as electromagnetic (EM) wave absorption materials, *Synth. Met.*, 2016, **221**, 291–298, DOI: [10.1016/j.synthmet.2016.09.018](#).
- 40 Y. Piao, V. N. Tondare, C. S. Davis, J. M. Gorham, E. J. Petersen, J. W. Gilman, *et al.*, Comparative study of multiwall carbon nanotube nanocomposites by Raman, SEM, and XPS measurement techniques, *Compos. Sci. Technol.*, 2021, **208**, 108753, DOI: [10.1016/j.compscitech.2021.108753](#).
- 41 B. Nandan, M. Bhatnagar and S. C. Kashyap, Cation distribution in nanocrystalline cobalt substituted nickel ferrites: X-ray diffraction and Raman spectroscopic investigations, *J. Phys. Chem. Solids*, 2019, **129**, 298–306, DOI: [10.1016/j.jpcs.2019.01.017](#).
- 42 K. Cao, X. Yang, R. Zhao and W. Xue, Fabrication of an ultralight Ni-MOF-RGO aerogel with both dielectric and magnetic performances for enhanced microwave absorption: microspheres with hollow structure grow onto the GO nanosheets, *ACS Appl. Mater. Interfaces*, 2023, **15**(7), 9685–9696, DOI: [10.1021/acsami.2c22935](#).
- 43 X. Di, Y. Wang, Z. Lu, R. Cheng and X. Wu, Design of biomass-derived magnetic carbon/polyaniline with hierarchical network for superior microwave absorption, *J. Mater. Sci.: Mater. Electron.*, 2021, **32**(14), 18790–18807, DOI: [10.1007/s10854-021-06397](#).
- 44 K. Peng, Y. Wu, G. Fang, G. Xu and C. Liu, Self-assembly hollow magnetoelectric composites emerging tunable property between microwave absorption and shielding with light-weight and broad bandwidth, *J. Alloys Compd.*, 2023, **947**, 169368, DOI: [10.1016/j.jallcom.2023.169368](#).
- 45 A. Katheria, P. Das, A. Bhagat, J. Nayak, S. Paul and N. Das, Fe<sub>3</sub>O<sub>4</sub>@g-C<sub>3</sub>N<sub>4</sub> and MWCNT embedded highly flexible polymeric hybrid composite for simultaneous thermal control and suppressing microwave radiation, *J. Alloys Compd.*, 2024, **988**, 174287, DOI: [10.1016/j.jallcom.2024.174287](#).
- 46 F. Fan, Z. Hu, Y. Ye and X. Liu, Preparation and Microwave Absorption Properties of Annular Fe<sub>3</sub>O<sub>4</sub>/RGO@ PANI, *JOM*, 2023, 1–11, DOI: [10.1007/s11837-023-05808-4](#).
- 47 J. Li, Y. Xie, W. Lu and T. W. Chou, Flexible electromagnetic wave absorbing composite based on 3D RGO-CNT-Fe<sub>3</sub>O<sub>4</sub> ternary films, *Carbon*, 2018, **129**, 76–84, DOI: [10.1016/j.carbon.2017.11.094](#).
- 48 Z. Wu, *et al.*, Honeycomb-like bamboo powders-derived porous carbon with low filler loading, high-performance microwave absorption, *Carbon*, 2023, **215**, 118415, DOI: [10.1016/j.carbon.2023.118415](#).
- 49 Y. Cao, A. M. Mohamed, M. Mousavi and Y. Akinay, Poly (pyrrole-co-styrene sulfonate)-encapsulated MWCNT/Fe–Ni alloy/NiFe<sub>2</sub>O<sub>4</sub> nanocomposites for microwave absorption, *Mater. Chem. Phys.*, 2021, **259**, 124169, DOI: [10.1016/j.matchemphys.2020.124169](#).
- 50 Z. Cai, Y. Ma, K. Zhao, M. Yun, X. Wang, Z. Tong, *et al.*, Ti<sub>3</sub>C<sub>2</sub>Tx MXene/graphene oxide/Co<sub>3</sub>O<sub>4</sub> nanorods aerogels with tunable and broadband electromagnetic wave absorption, *Chem. Eng. J.*, 2023, **462**, 142042, DOI: [10.1016/j.cej.2023.142042](#).
- 51 X. Zhou, Z. Jia, X. Zhang, B. Wang, X. Liu, B. Xu, *et al.*, Electromagnetic wave absorption performance of NiCo<sub>2</sub>X<sub>4</sub> (X= O, S, Se, Te) spinel structures, *Chem. Eng. J.*, 2021, **420**, 129907, DOI: [10.1016/j.cej.2021.129907](#).
- 52 F. Ebrahimi-Tazangi, S. H. Hekmatara and J. Seyed-Yazdi, Remarkable microwave absorption of GO-SiO<sub>2</sub>/Fe<sub>3</sub>O<sub>4</sub> via an effective design and optimized composition, *J. Alloys Compd.*, 2021, **854**, 157213, DOI: [10.1016/j.jallcom.2020.157213](#).
- 53 Q. Ren, T. Feng, Z. Song, P. Zhou, M. Wang, Q. Zhang, *et al.*, Autogenous and tunable CNTs for enhanced polarization and conduction loss enabling sea urchin-like Co<sub>3</sub>ZnC/Co/C composites with excellent microwave absorption performance, *ACS Appl. Mater. Interfaces*, 2022, **14**(36), 41246–41256, DOI: [10.1021/acsami.2c13064](#).
- 54 B. Dai, Y. Ma, S. Feng, H. Wang, M. Ma, J. Ding, X. Yin, *et al.*, Fabrication of one-dimensional M (Co, Ni)@ polyaniline nanochains with adjustable thickness for excellent microwave absorption properties, *J. Colloid Interface Sci.*, 2022, **627**, 113–125, DOI: [10.1016/j.jcis.2022.06.137](#).
- 55 Z. Fu, C. Lin and X. Meng, Three dimension Ni<sub>0.5</sub>Zn<sub>0.5</sub>Fe<sub>2</sub>O<sub>4</sub>/BaFe<sub>12</sub>O<sub>19</sub>@carbon composite for light weight, strong absorption and broadband microwave absorbents, *Ceram. Int.*, 2021, **47**(11), 16070–16078, DOI: [10.1016/j.ceramint.2021.02.181](#).
- 56 Y. Zhang, F. Dai, A. Hassan, M. R. A. Refaee, S. Salman, K. Nag, *et al.*, Investigations of microwave absorption performance of bi-layer absorber composed of FeWO<sub>4</sub> & BiVO<sub>4</sub> nanocomposite powder in 2–18 GHz, *J. Colloid Interface Sci.*, 2023, **641**, 1–14, DOI: [10.1016/j.jcis.2023.03.029](#).
- 57 J. Zhao, H. Wang, M. Chen, Y. Li, Z. Wang, C. Fang, *et al.*, Construct of CoZnO/CSP biomass-derived carbon composites with broad effective absorption bandwidth of 7.2 GHz and excellent microwave absorption performance, *J. Colloid Interface Sci.*, 2023, **639**, 160–170, DOI: [10.1016/j.jcis.2023.02.050](#).
- 58 S. Zhu, Y. Gau, H. Zhou, C. Zheng, X. Li, Q. Man, *et al.*, Expanded graphite/Co@ C composites with dual functions of corrosion resistance and microwave absorption, *J. Mater. Res. Technol.*, 2023, **23**, 3557–3569, DOI: [10.1016/j.jmrt.2023.02.005](#).
- 59 R. Zhang, D. Guo, Q. Liu, P. Yu, F. Wen, B. Wang, *et al.*, Engineering core-shell heterocomposites of integrated 0D ZIF-8 (Zn) attached on 1D MIL-68 (In) nanorods for high performance electromagnetic wave absorption, *Appl. Surf. Sci.*, 2023, **621**, 156898, DOI: [10.1016/j.apsusc.2023.156898](#).
- 60 X. Gao, X. Wang, J. Cai, Y. Zhang, J. Zhang, S. Bi, *et al.*, CNT cluster arrays grown on carbon fiber for excellent green EMI shielding and microwave absorbing, *Carbon*, 2023, **211**, 118083, DOI: [10.1016/j.carbon.2023.118083](#).
- 61 Q. Jiang, Y. Qiao, A. Uddin, X. Wu, F. Qin, H. Yi, *et al.*, Influence of impact on electromagnetic response of three-dimensional angle-interlock metacomposites, *Compos.*

- Commun.*, 2022, **30**, 101076, DOI: [10.1016/j.coco.2022.101076](#).
- 62 Q. Jiang, Y. Qiao, A. Uddin, F. Qin, L. Chen and L. Wu, Tailoring electromagnetic response of three-dimensional waffle-like metacomposite based on arrangement angle of ferromagnetic microwires, *Composites, Part B*, 2022, **247**, 110298, DOI: [10.1016/j.compositesb.2022.110298](#).
- 63 Y. Shen, Y. Wei, J. Ma, Y. Zhang, B. Ji, J. Tang, *et al.*, Self-cleaning functionalized FeNi/NiFe<sub>2</sub>O<sub>4</sub>/NiO/C nanofibers with enhanced microwave absorption performance, *Ceram. Int.*, 2020, **46**(9), 13397–13406, DOI: [10.1016/j.ceramint.2020.02.121](#).
- 64 B. Dai, F. Dong, H. Wang, Y. Qu, J. Ding, Y. Ma, *et al.*, Fabrication of CuS/Fe<sub>3</sub>O<sub>4</sub>@ polypyrrole flower-like composites for excellent electromagnetic wave absorption, *J. Colloid Interface Sci.*, 2023, **634**, 481–494, DOI: [10.1016/j.jcis.2022.12.029](#).
- 65 Y. Bai, L. He, P. Lv, C. Ge, H. Xu and X. Zhang, Impedance-matched (hydroxylated nano-BN/reduced graphene oxide) @ Fe<sub>3</sub>O<sub>4</sub>/polyaniline composite for efficient microwave absorption and thermal management, *Mater. Chem. Phys.*, 2023, **295**, 127193, DOI: [10.1016/j.matchemphys.2022.127193](#).
- 66 J. Xiao, B. Zhan, X. Qi, J. Ding, Y. Qu, X. Gong, J. Yang, L. Wang, W. Zhong and R. Che, Metal Valence State Modulation Strategy to Design Core@shell Hollow Carbon Microspheres@MoSe<sub>2</sub>/MoOx Multicomponent Composites for Anti-Corrosion and Microwave Absorption, *Small*, 2024, 2311312, DOI: [10.1002/sml.202311312](#).
- 67 G. Fang, Ch. Liu, M. Xu, X. Zhang, Y. Wu, D. H. Kim and G. Ji, The Elaborate Design of Multi-Polarization Effect by Non-Edge Defect Strategy for Ultra-Broad Microwave Absorption, *Adv. Funct. Mater.*, 2024, 2404532, DOI: [10.1002/adfm.202404532](#).
- 68 H. Zheng, K. Nan, Z. Lu, N. Nian Wang and Y. Wang, Core-shell FeCo@carbon nanocages encapsulated in biomass-derived carbon aerogel: Architecture design and interface engineering of lightweight, anti-corrosion and superior microwave absorption, *J. Colloid Interface Sci.*, 2023, **646**, 555–566, DOI: [10.1016/j.jcis.2023.05.076](#).